

# The $^1S_0$ - $^3P_2$ magnetic quadrupole transition in neutral strontium

J. Trautmann,<sup>1,2</sup> D. Yankelev,<sup>1,2</sup> V. Klüsener,<sup>1,2</sup> A. J. Park,<sup>1,2</sup> I. Bloch,<sup>1,3,2</sup> and S. Blatt<sup>1,3,2,\*</sup>

<sup>1</sup>Max-Planck-Institut für Quantenoptik, Hans-Kopfermann-Straße 1, 85748 Garching, Germany

<sup>2</sup>Munich Center for Quantum Science and Technology, 80799 München, Germany

<sup>3</sup>Fakultät für Physik, Ludwig-Maximilians-Universität München, 80799 München, Germany

(Dated: November 7, 2022)

We present a detailed investigation of the ultranarrow magnetic-quadrupole  $^1S_0$ - $^3P_2$  transition in neutral strontium and show how it can be made accessible for quantum simulation and quantum computation. By engineering the light shift in a one-dimensional optical lattice, we perform high-resolution spectroscopy and observe the characteristic absorption patterns for a magnetic quadrupole transition. We measure an absolute transition frequency of 446,647,242,704(5) kHz in  $^{88}\text{Sr}$  and an  $^{88}\text{Sr}$ - $^{87}\text{Sr}$  isotope shift of +62.93(6) MHz. In a proof-of-principle experiment, we use this transition to demonstrate local addressing in an optical lattice with 532 nm spacing with a Rayleigh-criterion resolution of 494(45) nm. Our results pave the way for applications of the magnetic quadrupole transition as an optical qubit and for single-site addressing in optical lattices.

Trapped ultracold two-electron atoms have emerged as a promising platform for metrology [1, 2], quantum simulation [3–5], and quantum computation [6–8]. One pillar of their success are their ultranarrow optical transitions between the singlet  $^1S_0$  ground state and the long-lived metastable triplet  $^3P_J$  states, as shown in Fig. 1.

The majority of the research in metrology, quantum simulation, and quantum computation with two-electron atoms relies on the  $^1S_0$ - $^3P_0$  clock transition, which is insensitive to most environmental effects. This transition is forbidden by spin and angular momentum selection rules. However, an electric dipole (E1) transition can be induced by hyperfine mixing [19] in fermionic isotopes with nuclear spin or by magnetic-field-induced mixing [15, 20–22] in bosonic isotopes without nuclear spin. On the clock transition, coherence times of tens of

seconds have been experimentally demonstrated [9–11], and it forms the basis of optical lattice clocks based on fermionic  $^{87}\text{Sr}$  [28, 29] and bosonic  $^{88}\text{Sr}$  [30–32]. Accordingly, the strontium clock transition has been thoroughly investigated [10, 11, 23–27],

In contrast to the clock transition, the  $^1S_0$ - $^3P_2$  transition in  $^{88}\text{Sr}$  can be driven even at zero magnetic field, because it is magnetic-quadrupole (M2) allowed [18]. This transition offers several attractive features for quantum science and technology. Because the  $^1S_0$  ground state has zero angular momentum, the Clebsch-Gordan coefficients of the transitions out of  $^1S_0$  to all Zeeman sublevels of any given excited state are equal. This property makes  $^{88}\text{Sr}$  an ideal atom to study fundamental light-matter interactions and for high-quality spectroscopy. In addition, the non-vanishing electronic angular momentum of  $^3P_2$  allows high flexibility in engineering the atomic polarizability [20, 21, 33]. The  $^3P_2$  state also possesses a large magnetic moment, allowing control over the excited state's energy with external magnetic fields. In combination with a natural lifetime of hundreds of seconds [34] this tunability provides new opportunities for quantum computing and quantum simulation [35, 36].

For example, the  $^1S_0$  state and the  $^3P_2$  Zeeman sublevels with  $m_J \neq 0$  support magnetically-sensitive transitions that can be used for single-site addressing in an optical lattice within a magnetic-field gradient [35–39]. Single-site addressing allows the manipulation and readout of quantum states on the level of single atoms and the preparation of a single lattice layer for a quantum gas microscope [39–41].

So far, the  $^1S_0$ - $^3P_2$  transition has been studied in quantum simulation experiments with Yb [8, 37–39, 42, 43]. Only very recently, a pioneering experiment measured the transition frequency in fermionic  $^{87}\text{Sr}$  with an uncertainty of 30 MHz [44].

In this article, we demonstrate the advantages of the ultranarrow  $^1S_0$ - $^3P_2$  M2 transition for quantum simulation and quantum computing with  $^{88}\text{Sr}$ . First, we present a theoretical framework of the selection rules and the transition amplitude's dependence on the light polariza-

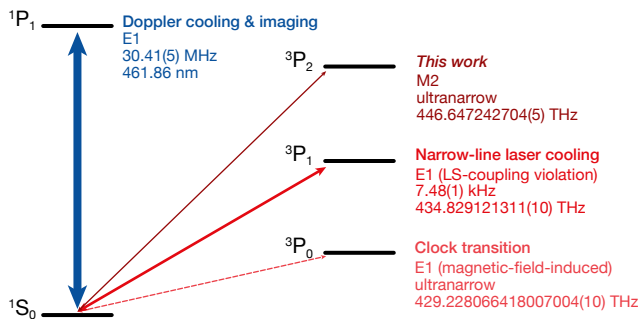


FIG. 1. Level diagram of  $^{88}\text{Sr}$  including the important optical transitions from the  $^1S_0$  ground state. The broad transition to  $^1P_1$  is electric-dipole (E1) allowed and is used for Doppler cooling and imaging. The intercombination transitions to the lowest  $^1P_J$  states should be electric-dipole forbidden. However, LS-coupling [12] is violated, which leads to a narrow E1 transition to  $^3P_1$  [13, 14], used for narrow-line laser cooling. The ultranarrow clock transition to the  $^3P_0$  state is doubly-forbidden, and only becomes E1-allowed by perturbatively mixing  $^3P_0$  with  $^3P_1$  via a bias magnetic field [15–17]. In contrast, the  $^1S_0$ - $^3P_2$  transition is magnetic-quadrupole (M2) allowed even at zero bias field [18].

tion and propagation direction for M2 transitions and compare these results to the well-known E1 transitions. We experimentally demonstrate this dependence for the  $^1S_0$ - $^3P_2$  transition in  $^{88}\text{Sr}$ . Second, we study the specific properties and applications of the  $^1S_0$ - $^3P_2$  transition in  $^{88}\text{Sr}$ . By engineering the polarizability of the  $^3P_2$  state via the trap polarization and the bias magnetic field, we perform Doppler- and Stark-shift-free spectroscopy for magnetic-field-insensitive and magnetic-field-sensitive transitions. We measure the absolute frequency of the  $^1S_0$ - $^3P_2$  transition in  $^{88}\text{Sr}$  and  $^{87}\text{Sr}$ , allowing us to extract the  $^{87}\text{Sr}$ - $^{88}\text{Sr}$  isotope shift. In a final proof-of-principle experiment, we demonstrate local addressing in an optical lattice with single-site resolution.

## I. MULTIPOLE TRANSITIONS

We are interested in describing the transition amplitude for a general multipole transition between an atomic ground state  $|J, m_J\rangle$  and an excited state  $|J', m'_J\rangle$ . For the well-known E1 transitions, several characteristics allow for a simplified description. Assuming a plane wave, only the photon's *spin* – its polarization – determines the change in the atom's orbital angular momentum. For example, when driving a transition that does not change the atom's magnetic sublevel ( $\Delta m_J \equiv m'_J - m_J = 0$ ), only the  $\pi$  polarization component will determine the transition amplitude. In addition, the amplitude of an E1 transition does not depend on the driving field's propagation direction  $\hat{\mathbf{k}}$ , beyond the constraints that it imposes on the polarization vector  $\hat{\boldsymbol{\epsilon}}$ .

These simplifications do not generally hold for higher-order multipole transitions, which also allow the transfer of additional *orbital* angular momentum besides the photon spin, including for a plane wave. Hence, all three polarization components can contribute to driving a certain transition, while the orbital angular momentum transfer satisfies the conservation of total angular momentum. Since the orbital angular momentum depends on the propagation direction, this direction now explicitly affects the transition amplitude resulting in an *angular dependence* [45] of the amplitude.

While the theory of atomic multipole transitions is well understood [46], the nuances of the contribution of the different polarization components and of the transition amplitude's angular dependence are rarely discussed. In this section, we present an overview of these dependencies to provide a convenient framework for our experimental work on the  $^1S_0$ - $^3P_2$  M2 transition.

We begin by reviewing the main results obtained from expanding the light-matter interaction Hamiltonian into multipole orders under simplifying assumptions, described in detail in Appendix A. Based on these results, we discuss the effects of the polarization and the angular dependence for a general multipole transition. Next, we focus on two specific multipole orders: the electric dipole, where we show that the transfer of orbital angular momentum and the angular dependence disappear as expected; and the magnetic quadrupole, the scenario of interest for the  $^1S_0$ - $^3P_2$  transition in two-electron atoms.

### A. General theory of multipole transitions

Optical atomic transitions result from the coupling of the electromagnetic vector potential  $\mathbf{A}$  with the atom's valence electrons and can be described by the interaction Hamiltonian

$$H_{\text{int}} = -\frac{e}{m_e} \mathbf{P} \cdot \mathbf{A} + g_B \mu_B (\nabla \times \mathbf{A}) \cdot \mathbf{S}, \quad (1)$$

in the Coulomb gauge [12, 47]. Here,  $\mu_B$  is the Bohr magneton,  $e$  is the charge,  $m_e$  is the mass, and  $g_B$  is the gyromagnetic ratio of an electron. The operator  $\mathbf{P}$  ( $\mathbf{S}$ ) is the total momentum (spin), summed over all valence electrons. This description assumes that the vector potential does not vary over the spatial extent of the atom.

The vector potential at the position of the atom can be expanded in different multipole orders  $K$  [46], where  $K = 1$  corresponds to the dipole terms,  $K = 2$  corresponds to the quadrupole terms, and so forth. In the multipole expansion, the interaction Hamiltonian separates into electric and magnetic parts  $H_{K,q}^{(\text{el})}$  and  $H_{K,q}^{(\text{mg})}$ , respectively. These terms contain spherical tensor operators [48] of rank  $K$  with components  $q = -K, \dots, +K$ . The natural frame to describe these tensors is in the basis consisting of the vectors  $\hat{\mathbf{e}}_0 = \hat{\mathbf{z}}$  and  $\hat{\mathbf{e}}_{\pm} = \mp(\hat{\mathbf{x}} \pm i\hat{\mathbf{y}})/\sqrt{2}$ , corresponding to the atomic-frame polarization components of  $\pi$ - and  $\sigma^{\pm}$ -polarization, respectively.

To obtain the specific form of the interaction Hamiltonian relevant for the experiments described in this work, we assume that the vector potential can be approximated by a plane wave with wave-vector  $\mathbf{k}$  and polarization  $\hat{\boldsymbol{\epsilon}}$ , such that  $\mathbf{k} \cdot \hat{\boldsymbol{\epsilon}} = 0$ . As shown in Appendix A, the multipole decomposition of a plane wave leads to the decomposition of the interaction Hamiltonian

$$H_{\text{int}} = 4\pi \sum_{K=1}^{\infty} \sum_{q=-K}^K i^K \left[ -i \left( \mathbf{Y}_{K,q}^{(\text{el})}(\hat{\mathbf{k}}) \cdot \hat{\boldsymbol{\epsilon}} \right) H_{K,q}^{(\text{el})} + \left( \mathbf{Y}_{K,q}^{(\text{mg})}(\hat{\mathbf{k}}) \cdot \hat{\boldsymbol{\epsilon}} \right) H_{K,q}^{(\text{mg})} \right], \quad (2)$$

into the multipole terms

$$H_{K,q}^{(\lambda)} = -\frac{e}{m_e} \mathbf{P} \cdot \mathbf{a}_{K,q}^{(\lambda)}(k, \mathbf{r}) + g_B \mu_B \mathbf{S} \cdot [\nabla \times \mathbf{a}_{K,q}^{(\lambda)}(k, \mathbf{r})], \quad (3)$$

corresponding to the electric ( $\lambda \rightarrow \text{el}$ ) and magnetic ( $\lambda \rightarrow \text{mg}$ ) interactions, respectively. Here,  $\mathbf{a}_{K,q}^{(\lambda)}$  is the coefficient corresponding to component  $q$  of the order- $K$  multipole expansion of  $\mathbf{A}$ , as described in Appendix A.

The multipole operator  $H_{K,q}^{(\lambda)}$  describes the light-atom interaction of a multipole transition, including all atomic

selection rules and Clebsch-Gordan coefficients. The Clebsch-Gordan coefficients for a transition between two atomic states  $|J, m_J\rangle$  and  $|J', m'_J\rangle$  can be derived from the matrix elements  $\langle J', m'_J | H_{K,q}^{(\lambda)} | J, m_J \rangle$ . Since the multipole operators are irreducible tensor operators [49, 50], the matrix element can be calculated using the Wigner-Eckart theorem [12, 45], leading to the selection rules  $|J' - J| \leq K \leq J' + J$ , and  $q = \Delta m_J$ .

The term  $\mathbf{Y}_{K,q}^{(\lambda)}(\hat{\mathbf{k}}) \cdot \hat{\epsilon}$  describes the transition amplitude's dependence on the light field propagation direction and its polarization, where  $\mathbf{Y}_{K,q}^{(\lambda)}(\hat{\mathbf{k}})$  are the vector spherical harmonics (see Appendix A) [46]. For the remainder of this section, we will focus on this dependence.

By decomposing the term describing the angular dependence into the atomic polarization basis  $\hat{\mathbf{e}}_s$ , we find

$$\mathbf{Y}_{K,q}^{(\text{el})}(\hat{\mathbf{k}}) \cdot \hat{\epsilon} = \sum_{s=-1}^1 \left[ c_{K,q,s}^{(-1)} Y_{K-1}^{q-s}(\hat{\mathbf{k}}) + c_{K,q,s}^{(+1)} Y_{K+1}^{q-s}(\hat{\mathbf{k}}) \right] (\hat{\mathbf{e}}_s \cdot \hat{\epsilon}), \quad (4)$$

$$\mathbf{Y}_{K,q}^{(\text{mg})}(\hat{\mathbf{k}}) \cdot \hat{\epsilon} = \sum_{s=-1}^1 c_{K,q,s}^{(0)} Y_K^{q-s}(\hat{\mathbf{k}}) (\hat{\mathbf{e}}_s \cdot \hat{\epsilon}), \quad (5)$$

where  $Y_K^q(\hat{\mathbf{k}})$  are the scalar spherical harmonics as a function of the unit vector  $\hat{\mathbf{k}}$ . The explicit values of the  $c_{K,q,s}^{(j)}$  coefficients for the dipole and quadrupole transitions are given in Appendix A.

From Eqs. (4) and (5), we observe that, in general, all three polarization components can contribute to the amplitude of a given transition, even if their polarization-determined spin  $s$  is different from the change in the electronic angular momentum  $q$ . To conserve angular momentum in such cases, the light field transfers  $q - s$  quanta of orbital angular momentum along the quantization axis. We further note the dependence of the transition strength on the direction of  $\hat{\mathbf{k}}$  of the light field given by  $Y_K^{q-s}(\hat{\mathbf{k}})$ .

## B. Angular dependence of E1 and M2 transitions

In the following, we specialize the general formalism to two scenarios of interest, the well-known E1 transition and the M2 transition relevant for our experimental studies. For an E1 transition, we show in Appendix A that the angular dependence in Eq. (4) simplifies to

$$\mathbf{Y}_{1,q}^{(\text{el})}(\hat{\mathbf{k}}) \cdot \hat{\epsilon} = \sqrt{\frac{3}{8\pi}} (\hat{\mathbf{e}}_q \cdot \hat{\epsilon}). \quad (6)$$

The contributions of the polarization components with  $s \neq q$  vanish, such that, *e.g.*, for  $q = 0$  only the  $\pi$  polarization component contributes to the transition amplitude. The explicit dependence on  $\hat{\mathbf{k}}$  also disappears. Hence, we recover the expected results from the standard

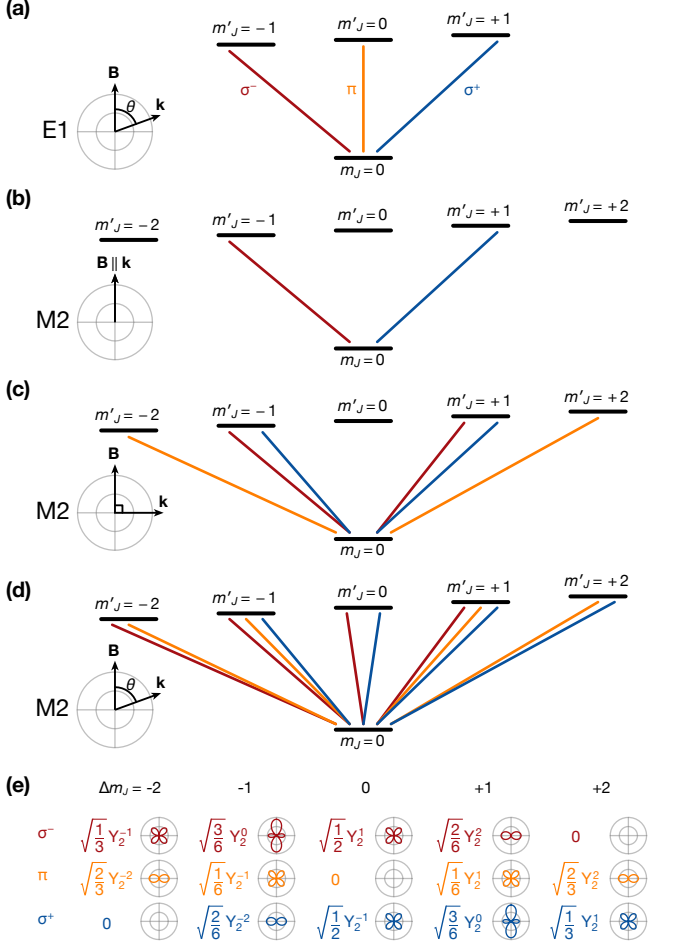


FIG. 2. The contributions of the atomic-frame light polarization components of the driving beam to the different  $\Delta m_J$  transitions, where the magnetic field  $\mathbf{B}$  defines the quantization axis. The full transition amplitude is obtained by decomposing the physical polarization and coherently summing the contributions from all components (phase information not depicted in figure). (a) The case of an E1 transition for  $J = 0$  and  $J' = 1$ . The  $\pi$  and  $\sigma^\pm$  polarizations drive only the  $\Delta m_J = 0$  and  $\pm 1$  transitions, respectively. The transition amplitude does not depend on the propagation direction beyond the constraints it imposes on the polarization. (b) An M2 transition driven by a probe beam propagating along the quantization axis for  $J = 0$  and  $J' = 2$ . As for the E1 transition,  $\sigma^\pm$  polarizations drive only  $\Delta m_J = \pm 1$ , respectively. (c) As in panel (b), but for propagation perpendicular to the quantization axis. Here both  $\sigma^\pm$  contribute to each of the  $\Delta m_J = \pm 1$  transitions, while the  $\pi$  polarization drives only the  $\Delta m_J = \pm 2$  transitions. (d) As in panel (c), but for an arbitrary relative angle  $\theta$  between propagation and quantization axis. Nearly all polarization components can contribute to all  $\Delta m_J$  transitions, with the transition amplitudes depending on  $\theta$ . (e) The angular dependence of the amplitudes of M2 transitions for each polarization and  $\Delta m_J$  as a function of  $\theta$ , as defined in panel (d).

dipole interaction Hamiltonian, visualized in Fig. 2(a) for a  $J = 0$  to  $J' = 1$  transition.

Next, we discuss in detail the M2 transition, the scenario of interest for the  $^1S_0$ - $^3P_2$  transition in  $^{88}\text{Sr}$ . For the relevant case of  $J = 0$  to  $J' = 2$ , all Clebsch-Gordan coefficients are equal, and only the angular dependence determines the relative transition strengths.

First, we can consider the limiting cases of the light field propagating parallel to the quantization axis or perpendicular to the quantization axis. For parallel propagation, the allowed transitions in Fig. 2(b) are similar to the ones of an E1 transition. However, the allowed transitions for perpendicular propagation shown in Fig. 2(c) are very different. In this case,  $\pi$  polarization only drives the  $\Delta m_J = \pm 2$  transitions, while the  $\Delta m_J = \pm 1$  transitions are each driven by both  $\sigma^\pm$ -polarization components.

The case of an arbitrary propagation direction is visualized in Fig. 2(d). For a given  $\Delta m_J$ , the transition amplitude will generally have contributions from all polarization components such that  $|s - \Delta m_J| \leq 2$ . This is as expected from a magnetic transition with  $K = 2$ , which can deliver up to 2 quanta of angular momentum. A notable exception is the  $\Delta m = 0$  transition, which cannot be driven with  $\pi$ -polarized light at all, despite not being forbidden by angular momentum considerations.

The relative magnitude of each polarization component's contribution to the transition amplitude into a specific Zeeman sublevel as a function of the propagation direction is plotted in Fig. 2(e). This visualization is meant to be used as follows. First, decompose the polarization vector into the spherical tensor basis  $\hat{e}_q$  [48]. Next, weight each row of Fig. 2(e) accordingly, and finally coherently sum over the rows. The angular dependencies apply to all M2 transitions, regardless of the values of  $J$  and  $J'$ . For  $J \neq 0$ , the calculation of the relative transition amplitudes only needs to be extended by taking into account the different Clebsch-Gordan coefficients. A detailed analysis is presented in Appendix A.

Note that the above derivations are based on plane waves under the assumption of transverse fields ( $\mathbf{k} \cdot \hat{e} = 0$ ). Our derivations can be extended to more general scenarios, such as strongly focused laser beams [51] and laser beams carrying orbital angular momentum [52–54].

## II. EXPERIMENTAL SETUP

High-resolution spectroscopy of an ultranarrow optical transition requires a long interrogation time and the suppression of systematic effects that lead to frequency shifts and line broadening, most notably the Doppler and ac Stark effects. For this reason, we perform the  $^1S_0$ - $^3P_2$  spectroscopy using a sample of ultracold strontium atoms trapped in an optical lattice.

For the measurements presented in this work, we prepare a sample of strontium  $^{88}\text{Sr}$  in a fast and dense magneto-optical trap [55] and then optically transport

it into the interrogation region [56] using a moving optical lattice [57]. In the interrogation region, we adiabatically load the atoms into a vertical, retro-reflected, one-dimensional (1D) optical lattice at 1064 nm, sketched in Fig. 3(a). We operate at sufficient lattice depth to suppress Doppler broadening in the Lamb-Dicke and resolved-sideband regimes [58]. The lattice polarization  $\hat{e}_l$  can be dynamically controlled by motorized wave-plates, allowing control over the excited-state polarizability, as will be explained in detail in the following sections. After loading, we cool the atoms to the axial vibrational ground state using direct sideband cooling on the  $^1S_0$ - $^3P_1$   $\Delta m_J = \pm 1$  transitions [56]. Typically, we achieve axial temperatures of  $\sim 1.5 \mu\text{K}$ , measured with time-of-flight expansion.

To probe the  $^1S_0$ - $^3P_2$  transition, we interrogate the atoms with the spectroscopy laser beam. The beam is derived from a diode laser stabilized to a reference cavity with a finesse of  $\sim 20,000$ , resulting in a laser linewidth on the order of 1 kHz. The spectroscopy beam propagation direction  $\hat{\mathbf{k}}$  is collinear with the vertical lattice  $\hat{\mathbf{k}}_l$  and is focused to a  $1/e^2$  waist of  $\sim 450 \mu\text{m}$  at the position of the atoms. The spectroscopy beam polarization  $\hat{e}$  is linear and fixed throughout all the measurements reported in this work. Typically, the spectroscopy is performed with a beam power of 25.8 mW, and interrogation times range from tens to hundreds of milliseconds.

After applying the spectroscopy pulse, we measure the number  $N_g$  of  $^1S_0$  ground state atoms with absorption imaging. Since the  $^3P_2$  state has a long natural lifetime [34], atoms excited to  $^3P_2$  do not spontaneously decay back to the ground state over the duration of the experiment. Hence, the spectroscopic signal manifests as a reduction of the  $^1S_0$  atom number. The excited atoms are lost from the trap through inelastic collisions between metastable triplet atoms [26, 30, 43, 56, 59]. To compensate for possible drifts in atom number, we interleave identical experiments, but with an off-resonant spectroscopy pulse. The atom number  $N_0$  measured in these reference measurements is used to normalize the baseline of the measured spectra.

Further details about the experimental setup and sequence can be found in Appendix B.

## III. QUADRUPOLE TRANSITION ANGULAR DEPENDENCE

We experimentally investigate the angular dependence of the  $^1S_0$ - $^3P_2$  M2 transition by varying the angle  $\theta$  between the quantization axis, defined by a bias magnetic field  $\mathbf{B}$ , and the probe beam propagation direction  $\hat{\mathbf{k}}$ .

In practice, we vary  $\theta$  by changing the direction of  $\mathbf{B}$ , while keeping all beam propagation directions and polarizations fixed, as sketched in Fig. 3(a). We use a bias field magnitude of 1 G, which splits the transition to each magnetic sublevel of the  $^3P_2$  state by 2.1 MHz, and use a linear lattice polarization  $\hat{e}_l$ .

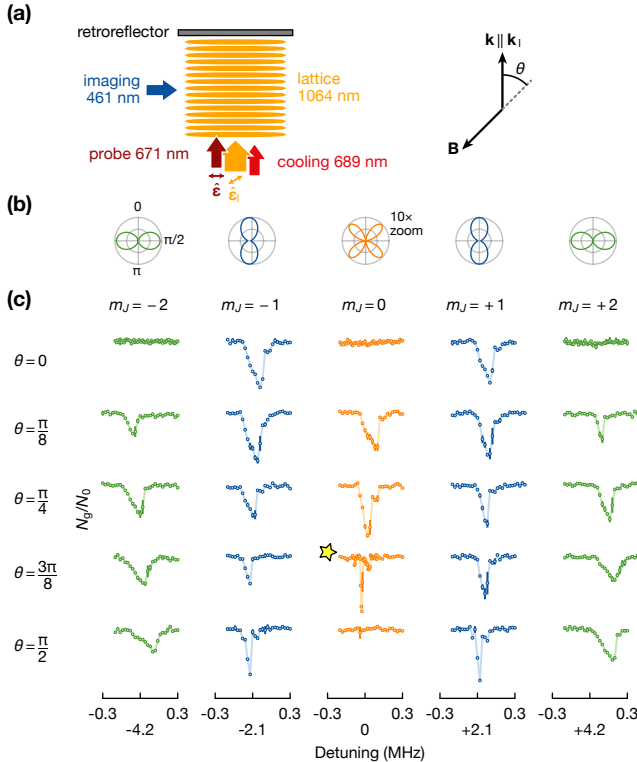


FIG. 3. Magnetic quadrupole transition in  $^{88}\text{Sr}$ . (a) Schematic of the experimental setup, including lattice (probe) wave vector  $\hat{\mathbf{k}}_l$  ( $\hat{\mathbf{k}}$ ) and magnetic field  $\mathbf{B}$  tilted at an angle  $\theta$ . The probe polarization  $\hat{\mathbf{e}}$  is linear with the major component in the plane spanned by  $\hat{\mathbf{k}}_l$  and  $\mathbf{B}$ ; the lattice polarization  $\hat{\mathbf{e}}_l$  is also linear. (b) Calculated transition amplitude's angular dependence as a function of  $\theta$  for the probe polarization  $\hat{\mathbf{e}}$  discussed in the main text. (c) Experimental study of the  $^1\text{S}_0$ - $^3\text{P}_2$  transition for all  $m_J$ -states as a function of  $\theta$ . The line strengths of the measured spectra follow the calculated patterns of panel (b), but the spectra are broadened due to the differential ac Stark shift of the  $^1\text{S}_0$  and the  $^3\text{P}_2$   $m_J$  states. The markers represent an average of 3 measurements, the error bars represent the standard error of the mean, and the solid lines are a guide to the eye.

We label the plane in which we vary  $\mathbf{B}$  in this measurement as the  $xz$ -plane, where the  $z$  is vertical. In this coordinate system, the probe polarization is oriented  $5^\circ$  from the  $x$  axis in the  $xy$ -plane. For this configuration, the  $\Delta m_J = 0$  transition is expected to be much weaker than the other transitions, since only the small out-of-plane  $y$  component contributes to driving the transition (see Appendix A). To ensure that even weak spectral features will be made visible, we choose a long interrogation time of 500 ms. We note that for an E1 transition, such a geometry would result in a significant transition amplitude for  $\Delta m_J = 0$  as  $\theta$  approaches  $\pi/2$ , since in the atomic frame the probe beam becomes predominantly  $\pi$ -polarized. Therefore, this choice of orientations allows us to discern the existence of possible E1 contributions to the transition amplitude.

In Fig. 3(b), we plot the expected absorption patterns as a function of  $\theta$ . The transition amplitude depends on  $\theta$  for each polarization both explicitly as described by Eq. (5) and visualized in Fig. 2(e), and implicitly through the change of the probe beam's polarization decomposition into the atomic frame. The experimental spectra of the individual  $^1\text{S}_0$ - $^3\text{P}_2$   $\Delta m_J$  transitions are shown in Fig. 3(c).

We observe spectra that are consistent with the expectations based on Fig. 3(b). First, for  $\theta = 0$ , we can only drive the transitions to the  $\Delta m_J = \pm 1$  states, as for an E1 transition with the same polarization. Next, for  $0 < \theta < \pi/2$ , we observe transitions to all excited states, including  $\Delta m_J = \pm 2$ , which are forbidden for an E1 transition. Finally, for  $\theta = \pi/2$ , we once again see a complete suppression of the  $\Delta m_J = 0$  transition, while still being able to drive  $\Delta m_J = \pm 2$ .

We also observe that each of the lines is broadened and shifted by the differential ac Stark shift of the  $^1\text{S}_0$  and  $^3\text{P}_2$  states, which depends on the  $^3\text{P}_2$  Zeeman sublevel and  $\theta$ . These light shifts complicate a quantitative analysis of the transition strengths in the general case. Nonetheless, the observed transition strengths qualitatively agree with the calculated M2 transition amplitude's angular dependence, allowing us to clearly see the unique properties of the M2 transition and how it differs from an E1 transition.

Considering the strong suppression of the  $\Delta m_J = 0$  transition at  $\theta = \pi/2$ , we conclude that at a magnetic field of 1 G, the transition is entirely due to M2 coupling, with a negligible E1 contribution (e.g. via state mixing). We further note that, in separate measurements, we tested the amplitude of the  $\Delta m_J = 1$  as a function of magnetic field magnitude up to 200 G at fixed  $\theta = 0$ , and observed no visible effect. From these experiments we conclude that the contribution of the E1 coupling due to state mixing is negligible compared to the M2 coupling, for a magnetic field of up to 200 G.

Finally, we note that the spectrum of the  $\Delta m_J = 0$  transition for  $\theta = 3\pi/8$ , marked with a star, is significantly less broadened than the other spectra presented in Fig. 3(c). It is sufficiently narrow to observe motional side bands at the trap frequency. Based on this observation, we engineer in the following sections Stark-shift-free experimental conditions for specific applications.

#### IV. MAGNETIC-FIELD-INSENSITIVE TRANSITION

As demonstrated in the previous section, high-precision spectroscopy in optical lattices requires understanding and control of the differential ac Stark shift. Differential Stark shifts can be suppressed by engineering the response of the atomic states involved in the transition. For the  $^1\text{S}_0$ - $^3\text{P}_0$  clock transition in Sr, this is typically done by working at the so-called “magic wavelength” around 813.4 nm [60, 61]. As we have observed in Fig. 3,

such a magic condition can also be found for the magnetically insensitive  $^1S_0-^3P_2$   $\Delta m_J = 0$  transition by tilting the magnetic field angle  $\theta$ .

In this section, we experimentally determine the magic field angle which allows us to measure the absolute frequency of the  $^1S_0-^3P_2$  transition in bosonic  $^{88}\text{Sr}$ . In a complementary measurement, we also find the absolute frequency of the  $^1S_0-^3P_2$  in fermionic  $^{87}\text{Sr}$  and extract the isotope shift.

### A. Tensor polarizability tuning

Stark shifts in high-resolution Doppler-free spectroscopy are well-understood [22, 61, 62]. Here, we briefly summarize the relevant information.

The Stark shift of an atomic level  $|i\rangle$  is proportional to the light intensity and the dynamic dipole polarizability  $\alpha_i$ . The polarizability can be decomposed into scalar, vector and tensor components [20, 22, 62], with different contributions depending on the Zeeman sublevel and the optical lattice polarization

$$\alpha_i(\lambda_l, \gamma, \theta) = \alpha_i^s(\lambda_l) + \alpha_i^v(\lambda_l) \sin(2\gamma) \frac{m_J}{2J} + \alpha_i^t(\lambda_l) \frac{3 \cos^2 \beta - 1}{2} \frac{3m_J^2 - J(J+1)}{2J(2J-1)}. \quad (7)$$

The coefficients  $\alpha_i^s$ ,  $\alpha_i^v$  and  $\alpha_i^t$  of the scalar, vector, and tensor terms, respectively, depend only on the atomic state and the wavelength of the optical lattice  $\lambda_l = 2\pi/k_l$ . The lattice polarization  $\hat{\mathbf{e}}_l$  is characterized by the angles  $\beta$  and  $\gamma$ , where  $\cos^2 \beta = |\hat{\mathbf{e}}_l \cdot \hat{\mathbf{B}}|^2$ , and  $\gamma$  is the ellipticity angle [20, 63]. We can write any elliptical lattice polarization as  $\hat{\mathbf{e}}_l = \cos \gamma \hat{\mathbf{e}}_{l,1} + i \sin \gamma \hat{\mathbf{e}}_{l,2}$ , where  $\hat{\mathbf{e}}_{l,1}$  and  $\hat{\mathbf{e}}_{l,2}$  are orthogonal basis vectors of the lattice polarization plane perpendicular to  $\mathbf{k}_l$ . For a linear lattice polarization,  $\beta$  is the angle between the polarization vector and the quantization axis, and  $\gamma = 0$ . A more detailed discussion can be found in Appendix D.

The vector and tensor polarizabilities of the  $^1S_0$  ground state vanish because  $J = 0$  and  $m_J = 0$ , and hence the ground state polarizability is independent of  $\beta$  and  $\gamma$ .

The results presented in section III serve as a good demonstration of tuning the tensor polarizability. In that measurement, we used a linearly polarized lattice, which resulted in a vanishing vector component also for the  $^3P_2$  state. The tensor polarizability of the  $^3P_2$  state does depend on  $\theta$ , as the rotation of the magnetic field also changes  $\beta$ , leading to different light shifts for each value of  $\theta$  and each  $m_J$  state.

This variation is most strongly apparent when considering the spectra for the  $\Delta m_J = 0$  transition in Fig. 3(d). As previously discussed, the linewidth of this transition changes dramatically as we vary  $\theta$ , reaching a narrow linewidth at  $\theta = 3\pi/8$  (marked with a star).

Varying  $\theta$  more finely around this value allows one to find the angle for which the differential ac Stark shift vanishes. Taking into account the precise orientation of

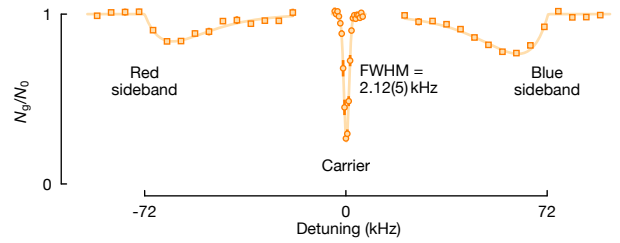


FIG. 4. Carrier (circles) and motional sidebands (squares) spectrum of the  $^1S_0-^3P_2$   $\Delta m_J = 0$  transition in a Stark-shift-free 1D optical lattice. The sidebands are probed for ten times longer than the carrier. The markers represent an average of 10 measurements, and the error bars are the standard error of the mean. The solid lines are fits, with the carrier fitted to a Gaussian and the sidebands to the sideband line shape discussed in Appendix C.

the lattice polarization  $\hat{\mathbf{e}}_l$ , we find that the “magic angle” for the  $^1S_0-^3P_2$   $\Delta m_J = 0$  transition is  $\beta_0 = 0.09(1)\pi$ , in excellent agreement with the theoretically expected value of  $0.089\pi$  (see Appendix D).

### B. Spectroscopy of the $\Delta m_J = 0$ transition

To find the absolute transition frequency, we probe the magnetic-field-insensitive  $^1S_0-^3P_2$   $\Delta m_J = 0$  transition in a Stark-shift-free lattice. We enhance the transition amplitude compared to the measurement performed in section III by rotating the magnetic field in the plane defined by  $(\hat{\mathbf{x}} + \hat{\mathbf{y}})/\sqrt{2}$  and  $\hat{\mathbf{z}}$  (see Appendix A).

At  $\beta_0$ , we probe the transition with an interrogation time of 35 ms as shown in Fig. 4. By fitting the carrier to a Gaussian lineshape, we extract a full-width-at-half-maximum (FWHM) linewidth of 2.12(5) kHz, confirming that our spectroscopy laser allows resolving spectral features on the kHz scale.

Due to the narrow transition linewidth, we can spectroscopically resolve the motional sidebands. At a detuning corresponding to the blue (red) sideband, atoms are transferred to higher (lower) vibrational states of the lattice. To compensate for the suppressed sideband amplitude in the Lamb-Dicke regime [33, 58], we probe the sidebands for 350 ms. We further enhance the red sideband by working with a hot atomic sample. The sideband spectrum of a cold sample can be found in Fig. 8 in Appendix C.

Finally, we use an optical frequency comb to obtain the absolute frequency of the spectroscopy laser at the carrier resonance conditions. We find the absolute transition frequency of the  $^1S_0-^3P_2$  transition in  $^{88}\text{Sr}$  to be 446, 647, 242, 704(5) kHz.

We additionally measure the absolute transition frequency for  $^{87}\text{Sr}$ . While the presented light-shift-engineering techniques also enable the realization of a Stark-shift-free lattice for the various states of  $^{87}\text{Sr}$ , we leave the determination of suitable magic conditions for

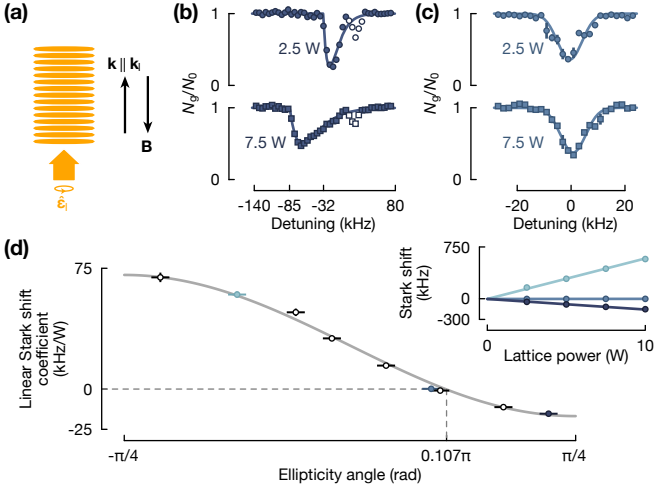


FIG. 5. Characterization of the vector ac Stark shift of the  $^1\text{S}_0-^3\text{P}_2 \Delta m_J = 1$  transition. (a) Simplified schematic of the experimental setup, emphasizing the differences compared to Fig 3(a). Here the magnetic field is oriented vertically, and the lattice polarization is elliptical. (b) Spectra in a lattice of elliptical polarization with an ellipticity angle of  $\gamma = 0.17\pi$  for a lattice power of 2.5 W (dots) and 7.5 W (squares). The sidebands (open markers) are excluded from the fit. The markers represent an average of 3 measurements, and the error bars are the standard error of the mean. The solid lines are fits to the expected ac-Stark-shift-broadened line shape as discussed in Appendix C. (c) As in panel (b), but for  $\gamma = 0.09\pi$ . The solid lines are Gaussian fits. (d) Differential ac Stark shift as a function of the ellipticity angle. To extract the magic ellipticity angle  $\gamma_0$ , we fit the data with the function  $a_0[\sin(2\gamma) - \sin(2\gamma_0)]$  (solid line), see Appendix D. The inset shows an example ac Stark shift measurements for three different elliptical lattice polarizations. We fit the data with a linear function, where the slope is the linear Stark shift coefficient. Vertical error bars represent  $1-\sigma$  uncertainty on the plotted parameter. Horizontal error bars represent the experimental uncertainty on the lattice polarization, discussed in Appendix D.

the spectroscopy for future work. Nonetheless, we find the frequency of the  $^1\text{S}_0-^3\text{P}_2 (F = 9/2)$  transition in  $^{87}\text{Sr}$  to be 446, 647, 798, 423(60) kHz. Taking into account the known hyperfine structure of  $^{87}\text{Sr}$  [76], our measurements leads to an isotope shift  $\nu(^{88}\text{Sr}) - \nu(^{87}\text{Sr}) = +62.93(6)$  MHz.

A detailed discussion of the spectroscopy and its uncertainties can be found in Appendix C.

## V. MAGNETIC-FIELD-SENSITIVE TRANSITION

Atoms trapped in optical lattices can be addressed and controlled by laser beams in combination with a magnetic field gradient that locally modifies the atomic resonance frequency [37, 39, 64]. This so-called local addressing enables controlling individual atomic qubits in quantum

computing schemes [36, 65]. The achievable spatial resolution is only limited by the strength of the gradient and the effective transition linewidth – taking into account all possible broadening mechanisms – and thus can allow super-resolution addressing beyond the diffraction limit.

Here, we use this technique to demonstrate how to isolate a single layer of a 1D optical lattice in the focus of a quantum gas microscope [38, 39, 66]. We aim to address only the atoms in a single lattice site using the magnetic-field-sensitive  $^1\text{S}_0-^3\text{P}_2 \Delta m_J = 1$  transition and a magnetic field gradient. The gradient splits the resonance frequencies of neighboring lattice layers by several tens of kHz, much larger than the broadening caused by environmental magnetic field noise which is on the scale of mG. To make the magnetic gradient uniform across the transverse extent of the optical lattice, we combine the gradient with a bias field on the order of 100 G pointing along the lattice.

For this technique to work, we need to engineer the differential ac Stark shift for this transition such that the linewidth becomes smaller than the frequency splitting between neighboring layers. However, since the bias magnetic field must point along the lattice, we cannot use it to tune the tensor polarizability as in Sec. IV. Instead, here we use the vector light shift and adjust the ellipticity angle  $\gamma$  of the lattice polarization in Eq. (7), until we find a “magic ellipticity”  $\gamma_0$  where the differential ac Stark shift vanishes.

### A. Vector polarizability tuning

As a first step, we investigate the differential light shift as a function of  $\gamma$ . We define the quantization axis by applying a static magnetic field of 20 G pointing along the  $-z$ -axis as indicated in Fig. 5(a). The wave vectors of the lattice and the probe beam are aligned parallel to the quantization axis. The lattice has an elliptical polarization described by  $\gamma$  in the  $xy$ -plane.

For a fixed ellipticity, we probe the spectrum of the  $^1\text{S}_0-^3\text{P}_2 \Delta m_J = 1$  transition for several lattice powers, as shown in Fig. 5(b). We observe a shift of the carrier frequency as a function of the lattice power and an asymmetric broadening of the line. Spectra with an ellipticity close to the Stark-shift-free condition at  $\gamma_0$  are shown in Fig. 5(c). The residual linewidth is determined by magnetic field fluctuations on the  $10^{-5}$  level.

To study the differential light shift, we extract the carrier frequencies by fitting the spectra with lineshapes discussed in Appendix C. For each value of  $\gamma$ , we find that the ac Stark shift changes linearly with the lattice power, with some examples plotted in the inset of Fig. 5(d). We plot the linear Stark shift coefficient as a function of the ellipticity angle  $\gamma$  in Fig. 5(d). By fitting these Stark-shift coefficients, we obtain the magic ellipticity angle  $\gamma_0 = 0.106(3)\pi$ . This value is in excellent agreement with the theoretical expectation of  $0.108\pi$ . In Appendix D, we show the corresponding polarizability cal-

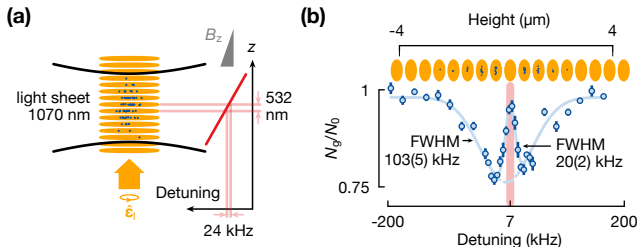


FIG. 6. (a) Simplified schematic of the experimental setup, emphasizing the differences compared to Fig 3(a). We compress the atomic cloud using a light sheet such that the atoms populate only a few lattice sites (left). With a magnetic field gradient of 215 G/cm we create a spatially-dependent Zeeman shift (right) that splits neighboring lattice sites by 24 kHz on the  $^1\text{S}_0$ - $^3\text{P}_2$   $\Delta m_J = 1$  transition. (b) Local addressing in an 1D optical lattice using the  $^1\text{S}_0$ - $^3\text{P}_2$  transition in a magnetic field gradient. The spectrum is broadened according to the spatial extent of the atomic cloud and the magnetic field gradient. Atoms in the layer that is resonant with the detuning of preparation pulse (red) are depleted prior to the spectroscopy, resulting in a dip in the spectrum at the appropriate detuning. The markers represent an average of 10 measurements, and the error bars are the standard error of the mean. The data is fitted to a broad Gaussian with a narrow Gaussian dip, with the solid (dashed) line representing the fitted curve with (without) the contribution of the narrow dip.

culations and provide further details on the experiments and their analysis.

### B. Local addressing

Finally, in a proof-of-principle experiment, we demonstrate local addressing on the  $^1\text{S}_0$ - $^3\text{P}_2$   $\Delta m_J = 1$  transition in a Stark-shift-free optical lattice at  $\gamma_0$  within a magnetic field gradient.

To reduce the number of initially populated lattice layers and thereby enhance the signal-to-noise ratio of the spectroscopic data, we compress the atomic cloud vertically using a light sheet before loading the atoms into the vertical lattice (see Appendix B). After this procedure, we obtain a significant atomic population over  $\sim 8$  lattice sites. Then, we apply a magnetic field gradient of 215 G/cm together with a bias magnetic field of 80 G along the  $-z$ -axis as shown in Fig. 6(a). This gradient splits the  $^1\text{S}_0$ - $^3\text{P}_2$   $\Delta m_J = 1$  resonance frequencies of neighboring layers by 24 kHz.

Then, we perform a “spectral hole burning” measurement. We address the atoms with a preparation pulse on the  $^1\text{S}_0$ - $^3\text{P}_2$  transition, followed by the spectroscopy sequence as in the previous sections. The corresponding spectrum is shown in Fig. 6(b). We use 300 ms-long and 200 ms-long pulses for preparation and spectroscopy, respectively.

The resulting spectrum is inhomogeneously broadened by the magnetic field gradient across the atomic sample to a FWHM  $> 100$  kHz. However, around the detuning

used for the preparation pulse, we observe a dip in the depletion curve. From this dip we infer that the preparation pulse indeed addressed and depleted the atoms only in a specific layer, while atoms in other layers were not influenced.

We characterize the spatial resolution corresponding to the narrow depletion dip of the cloud with the one-dimensional Rayleigh criterion, which requires the dip between the peaks of two Gaussians drop to 81% of the maximum [67]. If we apply this criterion to the observed depletion dip, we obtain a spatial resolution of 494(45) nm for the addressing pulse. This resolution should be sufficient to clearly resolve single lattice layers in the future, for which a more stable mechanical mounting of the lattice retro-reflector is needed. Our results pave the way to the preparation of a single lattice layer and to local addressing of qubits in quantum computing applications with neutral strontium atoms.

## VI. CONCLUSION

In this work, we demonstrate that the  $^1\text{S}_0$ - $^3\text{P}_2$  magnetic quadrupole transition in neutral strontium can be used as a precise tool for quantum simulation and quantum computation experiments. We present the first Doppler- and Stark-shift-free optical spectroscopy of this transition in bosonic  $^{88}\text{Sr}$  with kilohertz precision. We suppress differential light shifts by tuning the polarizability of the  $^3\text{P}_2$  state either by tilting the angle of the magnetic field with respect to the optical lattice or by adjusting the lattice polarization. We measure the absolute transition frequency to an accuracy of better than 10 kHz for  $^{88}\text{Sr}$  and to better than 100 kHz for  $^{87}\text{Sr}$ , orders-of-magnitude improvements over previous results [44, 68]. In addition, we present a theoretical framework and experimental demonstration of the polarization and propagation-direction dependence of the transition amplitude associated with a magnetic quadrupole transition, and high-order multipole transitions in general. Finally, in a proof-of-principle experiment, we locally address atoms in an optical lattice with a magnetic field gradient and demonstrate a spatial resolution at the half-micron scale.

The tunability of the  $^3\text{P}_2$  state with external fields and its ultranarrow transition linewidth offer advantages in controlling and manipulating excited state atoms for quantum simulation. The tunability of this state’s ac Stark shift allows generating Stark-shift-free lattices at 1064 nm, where high laser powers are readily available.

The magnetic field sensitivity of the  $^3\text{P}_2$  state also allows single-site addressing in an optical lattice within a magnetic field gradient which is impractical with the insensitive  $^3\text{P}_0$  state. This addressing enables the isolation of a single layer of an optical lattice required as a preparation step for quantum gas microscope experiments [40, 41, 69]. Furthermore, the scattering properties between  $^1\text{S}_0$  and  $^3\text{P}_2$  atoms can be tuned with a

magnetic field, enabling the search for magnetic Feshbach resonances in strontium, similar to those already observed in ytterbium [42].

The properties of the magnetically insensitive  $^1\text{S}_0$ - $^3\text{P}_2$   $\Delta m_J = 0$  transition create opportunities in quantum computation with alkaline earth atoms [8, 35, 36]. Our experiments demonstrate the first steps towards the full control over this transition, which can also serve as an optical qubit. One advantage of the M2 transition is that in bosonic isotopes the transition can be driven without applying a large magnetic field [15]. Recent theoretical proposals [70] to use the  $^3\text{P}_0$  and  $^3\text{P}_2$   $m_J = 0$  states as a fine-structure qubit for quantum computing highlight the need to investigate the  $^3\text{P}_2$  state in strontium experimentally. Being able to excite atoms to both  $^3\text{P}_2$  and  $^3\text{P}_0$  states paves the way to investigate the fine structure qubit built by these two states.

## ACKNOWLEDGMENTS

We thank M. Safronova for providing the matrix elements required for the polarizability calculation and T. Udem, S. Stellmer, and B. Ohayon for stimulating discussions. This work was supported by funding from the European Union (PASQuanS Grant No. 817482). A. J. P. was supported by a fellowship from the Natural Sciences and Engineering Research Council of Canada (NSERC), funding ref. no. 517029, and V. K. was supported by a Hector Fellow Academy fellowship.

## Appendix A: Multipole transition amplitudes

In this section, we present and expand on the derivation of the multipole decomposition of the light-matter interaction Hamiltonian in Eq. (1) that leads to the expressions in Eqs. (2) to (5).

### Full Hamiltonian

We begin the discussion by taking a closer look at the vector potential  $\mathbf{A}$ . We approximate the potential as a plane wave propagating along  $\mathbf{k}$ , such that  $\mathbf{A}(\mathbf{r}) = A_0 \hat{\epsilon} \exp(i\mathbf{k} \cdot \mathbf{r})$ , where  $\hat{\epsilon}$  is the polarization, the hat marks a unit vector, and  $A_0$  is the amplitude of the vector potential.

A natural approach would be to take advantage of the fact that the size of the atom is small compared to the wavelength of the laser beam, and expand the plane wave in terms of  $\mathbf{k} \cdot \mathbf{r} \ll 1$ . However, this procedure turns out to be inconvenient for the separation of the individual electric and magnetic higher-order multipole contributions [12].

Instead, we expand the vector potential in vector

spherical harmonics  $\mathbf{Y}_{Klq}$  [46]

$$\mathbf{Y}_{Klq}(\theta, \phi) = (-1)^{K-q} \sqrt{2K+1} \sum_{p=-1}^{+1} \begin{pmatrix} K & 1 & l \\ -q & p & q-p \end{pmatrix} Y_l^q(\theta, \phi) \hat{e}_p, \quad (\text{A1})$$

where the term in parentheses represents a Wigner-3j symbol. Then, the vector potential is given by

$$\mathbf{A}(\mathbf{r}) = \sum_{Klq} A_{Klq} \mathbf{Y}_{Klq}(\hat{\mathbf{r}}). \quad (\text{A2})$$

In the literature [46], the vector spherical harmonics are typically labeled with  $JLM$ . However, we choose the notation  $Klq$  to avoid confusion about the labels with the angular momentum of the relevant atomic states. To simplify the notation, we use the unit vector  $\hat{\mathbf{r}}$  as the argument of the vector spherical harmonics to represent the polar angles  $\theta_r$  and  $\phi_r$  describing the orientation of  $\mathbf{r}$ . Similarly, we use  $\hat{\mathbf{k}}$  to represent  $\theta$  and  $\phi$  below as in the main text. The expansion coefficients  $A_{Klq}$  can be determined from

$$A_{Klq} = A_0 \int_0^\pi \sin(\theta) d\theta \int_0^{2\pi} d\phi \times [(\mathbf{Y}_{Klq}(\hat{\mathbf{r}}) \cdot \hat{\epsilon}) \exp(i\mathbf{k} \cdot \mathbf{r})]. \quad (\text{A3})$$

Inserting the expansion of a plane wave in spherical harmonics  $Y_{lq}$  and spherical Bessel functions  $j_l$  [71]

$$\exp(i\mathbf{k} \cdot \mathbf{r}) = 4\pi A_0 \sum_{l,q} i^l j_l(kr) Y_{lq}^*(\hat{\mathbf{k}}) Y_{lq}(\hat{\mathbf{r}}), \quad (\text{A4})$$

we solve the integral in Eqn. (A3) and obtain [46]

$$\mathbf{A}(\mathbf{r}) = 4\pi A_0 \sum_{K,l,q} i^l (\mathbf{Y}_{Klq}(\hat{\mathbf{k}}) \cdot \hat{\epsilon}) j_l(kr) \mathbf{Y}_{Klq}(\hat{\mathbf{r}}). \quad (\text{A5})$$

Before we continue, we define another, more convenient, set of vector spherical harmonics  $\mathbf{Y}_{Kq}^{(\lambda)}$  [46]

$$\begin{aligned} \mathbf{Y}_{Kq}^{(-1)}(\hat{\mathbf{r}}) &= \sqrt{\frac{K}{2K+1}} \mathbf{Y}_{KK-1q}(\hat{\mathbf{r}}) - \sqrt{\frac{K+1}{2K+1}} \mathbf{Y}_{KK+1q}(\hat{\mathbf{r}}) \\ &= \frac{\mathbf{r}}{r} Y_K^q(\hat{\mathbf{r}}), \end{aligned} \quad (\text{A6})$$

$$\begin{aligned} \mathbf{Y}_{Kq}^{(0)}(\hat{\mathbf{r}}) &= \mathbf{Y}_{KKq}(\hat{\mathbf{r}}) \\ &= \frac{1}{\sqrt{K(K+1)}} \mathbf{L} Y_K^q(\hat{\mathbf{r}}), \end{aligned} \quad (\text{A7})$$

$$\begin{aligned} \mathbf{Y}_{Kq}^{(1)}(\hat{\mathbf{r}}) &= \sqrt{\frac{K+1}{2K+1}} \mathbf{Y}_{KK-1q}(\hat{\mathbf{r}}) + \sqrt{\frac{K}{2K+1}} \mathbf{Y}_{KK+1q}(\hat{\mathbf{r}}) \\ &= \frac{r}{\sqrt{K(K+1)}} \nabla Y_K^q(\hat{\mathbf{r}}). \end{aligned} \quad (\text{A8})$$

Using  $\mathbf{Y}_{Kq}^{(\lambda)}$ , the expansion of  $\mathbf{A}(\mathbf{r})$  becomes [46]

$$\mathbf{A}(\mathbf{r}) = 4\pi \sum_{Kq\lambda} i^{K-\lambda} (\mathbf{Y}_{Kq}^{(\lambda)}(\hat{\mathbf{k}}) \cdot \hat{\epsilon}) \mathbf{a}_{Kq}^{(\lambda)}(\hat{\mathbf{r}}), \quad (\text{A9})$$

with

$$\mathbf{a}_{Kq}^{(0)}(\hat{\mathbf{r}}) = A_0 j_K(kr) \mathbf{Y}_{Kq}^{(0)}(\hat{\mathbf{r}}), \quad (\text{A10})$$

$$\begin{aligned} \mathbf{a}_{Kq}^{(1)}(\hat{\mathbf{r}}) = A_0 & \left[ \sqrt{\frac{K+1}{2K+1}} j_{K-1}(kr) \mathbf{Y}_{KK-1q}(\hat{\mathbf{r}}) \right. \\ & \left. - \sqrt{\frac{K}{2K+1}} j_{K+1}(kr) \mathbf{Y}_{KK+1q}(\hat{\mathbf{r}}) \right]. \quad (\text{A11}) \end{aligned}$$

We identify the terms with  $\lambda = 0$  and  $\lambda = 1$  as the magnetic and electric multipole components, respectively [46]. This allows us to write  $\lambda = 0$  (1) or  $\lambda = mg$  (el), interchangeably. The term  $\mathbf{Y}_{Kq}^{(-1)}$  is parallel to  $\mathbf{k}$ , and thus its contribution vanishes under the assumption of  $\mathbf{k} \cdot \hat{\mathbf{e}} = 0$ .

Using the expansion of the vector potential, the light-matter interaction Hamiltonian in the Coulomb gauge becomes

$$\begin{aligned} H_{\text{int}} = 4\pi & \sum_{K,q,\lambda \in \{0,1\}} i^{K-\lambda} \left( \mathbf{Y}_{Kq}^{(\lambda)}(\hat{\mathbf{k}}) \cdot \boldsymbol{\epsilon} \right) \\ & \times \left( -\frac{e}{m_e} \mathbf{P} \cdot \mathbf{a}_{Kq}^{(\lambda)}(\hat{\mathbf{r}}) + g_B \mu_B \left[ \nabla \times \mathbf{a}_{Kq}^{(\lambda)}(\hat{\mathbf{r}}) \right] \cdot \mathbf{S} \right) \quad (\text{A12}) \end{aligned}$$

$$= 4\pi \sum_{K,q,\lambda \in \{0,1\}} i^{K-\lambda} \left( \mathbf{Y}_{Kq}^{(\lambda)}(\hat{\mathbf{k}}) \cdot \boldsymbol{\epsilon} \right) H_{K,q}^{(\lambda)}, \quad (\text{A13})$$

as presented in the main text.

### Atomic transition terms

*General expression.* — We can write the explicit expressions for the electric and magnetic contributions as [72]

$$H_{K,q}^{(\text{el})} = b_K k^K Q_{K,q}^{(\text{el})}(\mathbf{r}), \quad (\text{A14})$$

$$H_{K,q}^{(\text{mg})} = b_K k^K Q_{K,q}^{(\text{mg})}(\mathbf{r}), \quad (\text{A15})$$

with

$$b_K = \sqrt{\frac{(2K+1)(K+1)}{4\pi K}} \frac{1}{(2K+1)!!}, \quad (\text{A16})$$

$$Q_{K,q}^{(\text{el})}(\mathbf{r}) = e A_0 \sqrt{\frac{4\pi}{(2K+1)}} r^K Y_K^q(\hat{\mathbf{r}}), \quad (\text{A17})$$

$$\begin{aligned} Q_{K,q}^{(\text{mg})}(\mathbf{r}) = & \mu_B A_0 \sqrt{\frac{4\pi}{(2K+1)}} \nabla \left[ r^K Y_K^q(\hat{\mathbf{r}}) \right] \\ & \times \left( \frac{2}{K+1} \mathbf{L} + g_B \mathbf{S} \right), \quad (\text{A18}) \end{aligned}$$

where this definition of  $Q_{K,q}$  is chosen to be consistent with the literature on multipole transitions [49, 72].

*Selection rules and Clebsch-Gordan coefficients.* — Let us now consider an attempt to drive the atom from the state  $|i\rangle = |\gamma, J, m_J\rangle$  to the state  $|f\rangle = |\gamma', J', m'_J\rangle$ . Here,  $\gamma$  represents the state's radial wavefunction,  $J$  is its total angular momentum, and  $m_J$  is the projection of this angular momentum onto the quantization axis. Since  $Q_{K,q}^{(\text{el})}$  and  $Q_{K,q}^{(\text{mg})}$  are irreducible tensor operators of rank  $K$  [49, 50], we can use the Wigner-Eckart theorem [12, 45] to obtain

$$\begin{aligned} \langle f | Q_{K,q}^{(\text{el,mg})} | i \rangle = & (-1)^{J'-m'} \begin{pmatrix} J' & K & J \\ -m' & q & m \end{pmatrix} \\ & \times \langle \gamma', J' | Q_K^{(\text{el,mg})} | \gamma, J \rangle, \quad (\text{A19}) \end{aligned}$$

where  $\langle \gamma', J' | Q_K^{(\text{el,mg})} | \gamma, J \rangle$  is the reduced matrix element. This procedure leads to the standard angular momentum selection rules tying  $(K, q)$  to  $(J, J', m_J, m'_J)$  as described in the main text.

Taking into account the conservation of parity leads to additional selection rules. Substituting  $\mathbf{r} \rightarrow -\mathbf{r}$  into Eqs. (A17) and (A18), we find that the electric multipole operator  $Q_{K,q}^{(\text{el})}$  has a parity of  $(-1)^K$ , while the magnetic multipole operator  $Q_{K,q}^{(\text{mg})}$  has a parity of  $(-1)^{K+1}$ . In other words, states with identical parity can be coupled by electric transitions with even  $K$  and magnetic transitions with odd  $K$ ; conversely, states with opposite parity can be coupled by electric transitions with odd  $K$  and magnetic transitions with even  $K$ .

*Transitions in two-electron atoms.* — We now apply these rules to understand the important transitions from the ground-state, shown in Fig. 1, in two-electron atoms without nuclear spin, such as  $^{88}\text{Sr}$ .

We note that the  $^1\text{S}_0$  state has  $J = 0$ , and thus only the terms with  $K = J'$  can contribute. Since  $K \geq 1$ , the  $^1\text{S}_0$ - $^3\text{P}_0$  transition cannot be driven at all. For  $^1\text{P}_1$  and  $^3\text{P}_1$ , we can have only a dipole transition ( $K = 1$ ). Because the parity of the ground and excited states is opposite, it has to be an E1 transition. This is indeed the case for the  $^1\text{S}_0$ - $^1\text{P}_1$  transition, which is a strong E1-allowed transition. In contrast, the  $^1\text{S}_0$ - $^3\text{P}_1$  transition is forbidden by another selection rule arising from Eq. (A17): the electric transition operators  $Q_{K,q}^{(\text{el})}$  do not couple to the electronic spin and thus cannot change the spin quantum number.

The  $^1\text{S}_0$ - $^3\text{P}_1$  and  $^1\text{S}_0$ - $^3\text{P}_0$  transitions are only allowed due to state mixing in heavy atoms: the bare LS-coupling  $^3\text{P}_1^0$  state is mixed with the bare  $^1\text{P}_1^0$  state through LS-coupling violation [19], and the bare  $^3\text{P}_0^0$  state can be mixed with the  $^3\text{P}_1$  state by applying external magnetic fields [15] or via hyperfine coupling in the fermionic isotope [19]. State-mixing effects relate to the Hamiltonian of the unperturbed atom, rather than to the interaction Hamiltonian, and thus they are outside the scope of the derivations presented here. In summary, the  $^1\text{S}_0$ - $^3\text{P}_1$  and  $^1\text{S}_0$ - $^3\text{P}_0$  transitions are fundamentally related to the  $^1\text{S}_0$ - $^1\text{P}_1$  transition, and thus have E1 characteristics.

Applying the same considerations to the  $^1\text{S}_0$ - $^3\text{P}_2$  transition, the transition must have a quadrupole character

( $K = 2$ ), and from parity considerations it must be a magnetic quadrupole transition. Unlike the previous cases, this transition can be driven directly, even without considering state mixing. However, as for the  $^1S_0$ - $^3P_0$  transition, it is possible to induce an E1 contribution by an external magnetic field. As discussed in the main text, we find that for fields up to 200 G this effect is negligible, and the transition can be considered to be entirely M2.

### Angular dependence terms

We now discuss the transition amplitude's angular dependence described by the terms  $\mathbf{Y}_{K,q}^{(\lambda)}(\hat{\mathbf{k}}) \cdot \hat{\epsilon}$ . Substituting the definitions of the vector spherical harmonics presented above into this expression, we obtain the expressions presented in Eqs. (4) and (5) in the main text.

In Tab. I, we present the explicit values of the decomposition coefficients  $c_{K,q,s}^{(j)}$  for the first two orders corresponding to E1, M1, E2, and M2 transitions.

*Coordinate system.* — Here, we define the natural coordinate system used to calculate the transition amplitude's angular dependence. This coordinate system is illustrated in Fig. 7(a) and begins with the  $z$  axis that is already set by our choice of the quantization axis. We find that choosing the direction of  $x$  such that  $\mathbf{k}$  is contained in the  $xz$  plane is convenient, since then the spherical harmonics  $Y_K^q(\theta, \phi = 0)$  are real. This choice results in the fact that explicitly complex terms only occur in the polarization decomposition terms  $\hat{\epsilon}_s \cdot \hat{\epsilon}$ . Next, we decompose a linear polarization vector into the out-of-plane  $\hat{\epsilon}_1$  component (along  $\hat{\mathbf{y}}$ ) and the in-plane component  $\hat{\epsilon}_2$  (in the  $xz$  plane). The orientation of  $\mathbf{k}$  in the  $xz$  plane is defined by  $\theta$ , and the orientation of  $\hat{\epsilon}$  in the plane spanned by  $\hat{\epsilon}_1$  and  $\hat{\epsilon}_2$  is defined by  $\rho$ . Explicitly, we find

$$\begin{aligned} \mathbf{B} &= B\hat{\mathbf{z}}, \\ \mathbf{k} &= k(\cos\theta\hat{\mathbf{z}} + \sin\theta\hat{\mathbf{x}}), \\ \hat{\epsilon}_1 &= \hat{\mathbf{y}}, \\ \hat{\epsilon}_2 &= \sin\theta\hat{\mathbf{z}} - \cos\theta\hat{\mathbf{x}}, \\ \hat{\epsilon} &= \sin\rho\hat{\epsilon}_1 + \cos\rho\hat{\epsilon}_2. \end{aligned} \quad (\text{A20})$$

*Simplification of E1 transition amplitude's angular dependence.* — Considering the results in Tab. I, it appears at first glance as if the behavior of the E1 transition is more complex than expected, with possible contributions from all polarization components to each transition. However, we find that we can simplify the expressions to obtain the well-known picture presented in Fig. 2(a).

Let us consider the scenario for a general polarization vector  $\hat{\epsilon} = \alpha\hat{\epsilon}_1 + \beta\hat{\epsilon}_2$ , such that  $\alpha$  and  $\beta$  are complex coefficients satisfying  $|\alpha|^2 + |\beta|^2 = 1$  (the Jones vector).

TABLE I. Angular dependence coefficients  $c_{K,q,s}^{(j)}$  in Eqs. (4) and (5) for electric dipole (E1), magnetic dipole (M1), electric quadrupole (E2), and magnetic quadrupole (M2) transitions.

		$s = -1$ $\sigma^-$	$s = 0$ $\pi$	$s = +1$ $\sigma^+$
$Y_0^{q-s}$	$q = -1$	$c_{1,-1,s}^{(-1)}$	$\sqrt{\frac{20}{30}}$	0
	$q = 0$	$c_{1,0,s}^{(-1)}$	0	$\sqrt{\frac{20}{30}}$
	$q = 1$	$c_{1,1,s}^{(-1)}$	0	$\sqrt{\frac{20}{30}}$
$Y_2^{q-s}$	$q = -1$	$c_{1,-1,s}^{(+1)}$	$\sqrt{\frac{1}{30}}$	$-\sqrt{\frac{3}{30}}$
	$q = 0$	$c_{1,0,s}^{(+1)}$	$-\sqrt{\frac{3}{30}}$	$-\sqrt{\frac{4}{30}}$
	$q = 1$	$c_{1,1,s}^{(+1)}$	$\sqrt{\frac{6}{30}}$	$-\sqrt{\frac{3}{30}}$
$Y_1^{q-s}$	$q = -1$	$c_{1,-1,s}^{(0)}$	$\sqrt{\frac{1}{2}}$	$-\sqrt{\frac{1}{2}}$
	$q = 0$	$c_{1,0,s}^{(0)}$	$\sqrt{\frac{1}{2}}$	0
	$q = 1$	$c_{1,1,s}^{(0)}$	0	$\sqrt{\frac{1}{2}}$
$Y_1^{q-s}$	$q = -2$	$c_{2,-2,s}^{(-1)}$	$\sqrt{\frac{3}{5}}$	0
	$q = -1$	$c_{2,-1,s}^{(-1)}$	$\sqrt{\frac{3}{10}}$	$\sqrt{\frac{3}{10}}$
	$q = 0$	$c_{2,0,s}^{(-1)}$	$\sqrt{\frac{1}{10}}$	$\sqrt{\frac{2}{5}}$
	$q = 1$	$c_{2,1,s}^{(-1)}$	0	$\sqrt{\frac{3}{10}}$
	$q = 2$	$c_{2,2,s}^{(-1)}$	0	$\sqrt{\frac{3}{5}}$
$Y_3^{q-s}$	$q = -2$	$c_{2,-2,s}^{(+1)}$	$\sqrt{\frac{2}{105}}$	$-\sqrt{\frac{2}{21}}$
	$q = -1$	$c_{2,-1,s}^{(+1)}$	$\sqrt{\frac{2}{35}}$	$-\sqrt{\frac{16}{105}}$
	$q = 0$	$c_{2,0,s}^{(+1)}$	$\sqrt{\frac{4}{35}}$	$-\sqrt{\frac{6}{35}}$
	$q = 1$	$c_{2,1,s}^{(+1)}$	$\sqrt{\frac{4}{21}}$	$-\sqrt{\frac{16}{105}}$
	$q = 2$	$c_{2,2,s}^{(+1)}$	$\sqrt{\frac{2}{7}}$	$-\sqrt{\frac{2}{21}}$
$Y_2^{q-s}$	$q = -2$	$c_{2,-2,s}^{(0)}$	$\sqrt{\frac{1}{3}}$	$-\sqrt{\frac{2}{3}}$
	$q = -1$	$c_{2,-1,s}^{(0)}$	$\sqrt{\frac{3}{6}}$	$-\sqrt{\frac{1}{6}}$
	$q = 0$	$c_{2,0,s}^{(0)}$	$\sqrt{\frac{1}{2}}$	0
	$q = 1$	$c_{2,1,s}^{(0)}$	$\sqrt{\frac{2}{6}}$	$-\sqrt{\frac{1}{6}}$
	$q = 2$	$c_{2,2,s}^{(0)}$	0	$\sqrt{\frac{2}{3}}$
$Y_2^{q-s}$	$q = -2$	$c_{2,-2,s}^{(-1)}$	$\sqrt{\frac{2}{3}}$	$-\sqrt{\frac{1}{3}}$
	$q = -1$	$c_{2,-1,s}^{(-1)}$	$\sqrt{\frac{3}{6}}$	$-\sqrt{\frac{1}{6}}$
	$q = 0$	$c_{2,0,s}^{(-1)}$	$\sqrt{\frac{1}{2}}$	0
	$q = 1$	$c_{2,1,s}^{(-1)}$	$\sqrt{\frac{2}{6}}$	$-\sqrt{\frac{1}{6}}$
	$q = 2$	$c_{2,2,s}^{(-1)}$	0	$\sqrt{\frac{2}{3}}$

Then, the angular dependency is given by

$$|\mathbf{Y}_{1,0} \cdot \hat{\epsilon}|^2 = \frac{3}{8\pi} \beta\beta^* \sin^2\theta, \quad (\text{A21})$$

$$|\mathbf{Y}_{1,\pm 1} \cdot \hat{\epsilon}|^2 = \frac{3}{16\pi} (\alpha \pm i\beta \cos\theta) (\alpha^* \mp i\beta^* \cos\theta). \quad (\text{A22})$$

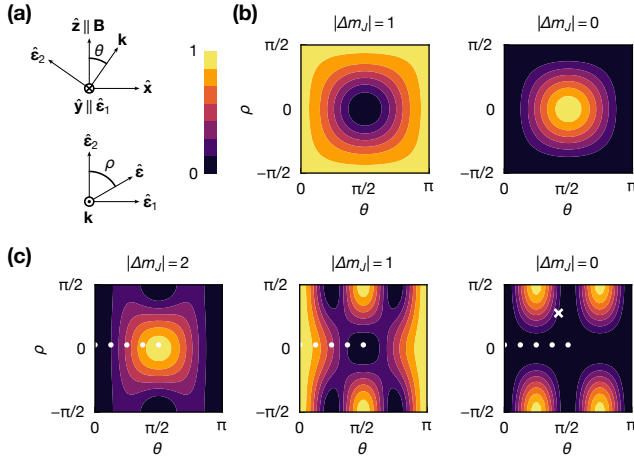


FIG. 7. (a) The coordinate system defined in this section.  $\mathbf{B}$  sets the  $z$  axis,  $\mathbf{k}$  and  $\hat{\epsilon}_2$  are in the  $xz$  plane,  $\hat{\epsilon}_1$  is along the  $y$  axis.  $\hat{\epsilon}$  is found in the plane spanned by  $\hat{\epsilon}_{1,2}$ . (b) The total angular dependence of E1 transition for linear polarization as a function of  $\theta, \rho$  as defined in (a), for the different possible  $|\Delta m_J|$  values this transition can drive (since it is linear, it is independent of the sign of  $\Delta m_J$ ). The dependence we observe is entirely due to the decomposition to the basis vectors. (c) like (b), for M2 transition. Here the dependence is more complicated and cannot be entirely attributed to the decomposition. The dots mark the  $(\theta, \rho)$  pairs corresponding to the measurements in section III. The cross marks the values corresponding to the measurement in section IV. The measurements in section V were performed for  $\theta = 0$ .

However, we notice that

$$|\hat{\mathbf{e}}_0 \cdot \hat{\mathbf{e}}|^2 = \beta \beta^* \sin^2 \theta, \quad (\text{A23})$$

$$|\hat{\mathbf{e}}_{\pm 1} \cdot \hat{\mathbf{e}}|^2 = \frac{1}{2} (\alpha \pm i \beta \cos \theta) (\alpha^* \mp i \beta^* \cos \theta). \quad (\text{A24})$$

Hence, we can substitute the full expression for  $\mathbf{Y}_{1,0} \cdot \hat{\mathbf{e}}$  with  $\sqrt{3/(8\pi)} \hat{\mathbf{e}}_q \cdot \hat{\mathbf{e}}$ , and thus are justified to consider the E1 transition amplitude's angular dependence as presented in Fig. 2(a).

*Complete transition amplitude's angular dependence.* — In Fig. 7, we plot the complete transition amplitude's angular dependence, assuming a linear polarization, for E1 and M2 transitions in panels (b) and (c), respectively. The complete angular dependence includes, on top of the explicit angular dependence discussed above, also the trivial dependence due to the decomposition into the polarization basis. In this sense, the dependence is different from the information plotted in Fig. 2, and similar to Fig. 3(b).

The coordinate system is defined such that  $\rho = 0$  means that the polarization is always in-plane relative to  $\mathbf{B}$  and  $\mathbf{k}$ . For this value of  $\rho$  and for changing  $\theta$  from 0 to  $\pi/2$ , the polarization starts from the sum of  $\sigma^\pm$  with equal phases and ends with  $\pi$ . Conversely,  $\rho = \pi/2$  means the polarization is fixed at a sum of  $\sigma^\pm$  with opposite phases.

For an E1 transition, we once again can see the ex-

pected behavior as a function of the two angles. For out-of-plane polarization, we drive only the  $\Delta m_J = \pm 1$  transition with a fixed amplitude. For in-plane polarization, we change from driving the  $\Delta m_J = \pm 1$  transition to driving the  $\Delta m_J = 0$  transition, corresponding exactly to the change of polarization from the sum of  $\sigma^\pm$  to  $\pi$ . The sum of the  $\sigma^\pm$  polarizations drives the  $\Delta m_J = \pm 1$  transitions with equal amplitude, regardless of the relative phase between them.

For the M2 transition, the pattern cannot be simplified by only considering the polarization projections. We can once again identify the properties we understood from Fig. 2 in the main text. Additionally, we observe a strong dependence on the relative phases between the contributions of the different polarization components. For example, for  $\Delta m_J = 0$ , we see that the in-plane polarization cannot drive the transition for any value of  $\theta$ . We already knew that the  $\pi$  polarization cannot drive this transition at all. For the sum of  $\sigma^\pm$ , we attribute the vanishing transition amplitude to the destructive interference between the contributions of the individual  $\sigma^\pm$  components.

We mark in Fig. 7(c) the conditions of the measurements reported in Sections III and IV.

Finally, we note that the complete angular dependence for electric and magnetic multipole transitions of the same order is identical, up to a shift of  $\rho$  by  $\pi/2$ . This can be intuitively understood by considering that the magnetic field orientation is simply perpendicular to the electric field within the polarization plane.

## Appendix B: Experimental setup

*Optical transport.* — We transport the atoms from the magneto-optical trap (MOT) region into a second vacuum chamber. For this purpose, we combine a traveling-wave optical lattice [57] with a focus-tunable optical dipole trap [73], so that we move the lattice nodes and the focal position synchronously [74]. The moving lattice allows for fast transport due to its deep longitudinal confinement, while the dipole trap supports the atoms against gravity. With this setup we can transport the atoms within 600 ms over a distance of about 55 cm.

*Vertical lattice.* — After the transport, we adiabatically load the atomic sample into the vertical 1D optical lattice. We derive the vertical lattice beam from a high-power fiber amplifier and focus the beam to a  $1/e^2$  waist of 144  $\mu\text{m}$  at the position of the atoms. With a typical power of 5 W, the lattice has a trap depth of 33  $\mu\text{K}$  and an axial trap frequency of 72 kHz corresponding to a Lamb-Dicke parameter  $\eta \simeq 0.21$  [33]. Motorized half-wave and quarter-wave plates allow us to dynamically adjust the lattice polarization, even during an experimental sequence.

Since the trap frequency is much larger than the  $^1\text{S}_0$ - $^3\text{P}_1$  linewidth, we can perform direct sideband cooling along the axial direction of the lattice. The cooling beam is aligned collinearly with the lattice beam. We apply a

bias magnetic field of 1 G pointing along the  $-z$ -axis to define the quantization axis. To optimize the cooling efficiency, we set the lattice polarization to an ellipticity angle of  $0.17\pi$ , making it magic for one  $m_J$  state of the  $^1\text{S}_0-^3\text{P}_1$  transition. With this method, we typically reach a vertical temperature of  $\sim 1.5\ \mu\text{K}$ .

We typically load about  $10^6$   $^{88}\text{Sr}$  atoms in the lattice, corresponding to up to 40,000 atoms per lattice layer.

*Spectroscopy laser.* — For the  $^1\text{S}_0-^3\text{P}_2$  spectroscopy, we use a home-built diode laser operating at 671 nm. The laser is stabilized to a reference cavity with a finesse of 25,000 using the Pound-Drever-Hall technique. The cavity is kept under vacuum of  $10^{-8}$  mbar and is temperature stabilized at the zero-crossing temperature of the ultra-low-expansion glass cavity spacer. The polarization of the beam is fixed for all experiments reported here. It is to a good approximation linear (ellipticity of  $0.06\pi$ ), and oriented  $5^\circ$  with respect to the  $x$  axis.

*Absolute frequency measurements.* — We use a few mW of the spectroscopy laser power to beat it with a commercial frequency comb, which is referenced to a hydrogen maser. The resulting beat frequency is measured with a counter. By averaging about 1000 counts, we obtain the beat frequency with an uncertainty of a few tens of Hz, given by the standard error of the mean.

*Compression in light sheet.* — To improve the signal-to-noise ratio (SNR) in the local addressing measurement, we decrease the number of vertical lattice sites populated by atoms. For this purpose, we spatially compress the atomic sample after the transport using a tightly focused optical dipole trap. We adiabatically load the atoms from the transport lattice into the dipole trap propagating along the  $y$  axis. The dipole trap is formed by a 1070 nm beam focused to an elliptical light sheet. The light sheet has a  $1/e^2$  waist of  $\sim 15\ \mu\text{m}$  ( $\sim 300\ \mu\text{m}$ ) along the  $z$ -axis ( $x$ -axis) and a power of 40 W, resulting in a vertical trap frequency of 2.2 kHz. We cool the atoms via Doppler cooling on the  $^1\text{S}_0-^3\text{P}_1$  transition. We reach near-magic condition for the cooling transition by setting the bias magnetic field of 1 G along the  $y$  axis and using circularly polarized light for the dipole trap. After cooling, we typically obtain a vertical temperature of  $\sim 0.6\ \mu\text{K}$ . Then, we adiabatically transfer the atoms from the sheet to the vertical lattice. The compression stage results in about eight lattice layers being significantly populated.

### Appendix C: Spectroscopy

*Spectral line shapes.* — At a finite atomic temperature, a differential light shift between two atomic states leads to an asymmetric broadening of the spectral line, as some atoms experience lower trapping intensity than others. The resulting line shape has been derived to be [20, 58, 75]

$$y(\delta) = y_0 - a(\delta - \delta_0)e^{-b(\delta - \delta_0)}\Theta(\delta - \delta_0), \quad (\text{C1})$$

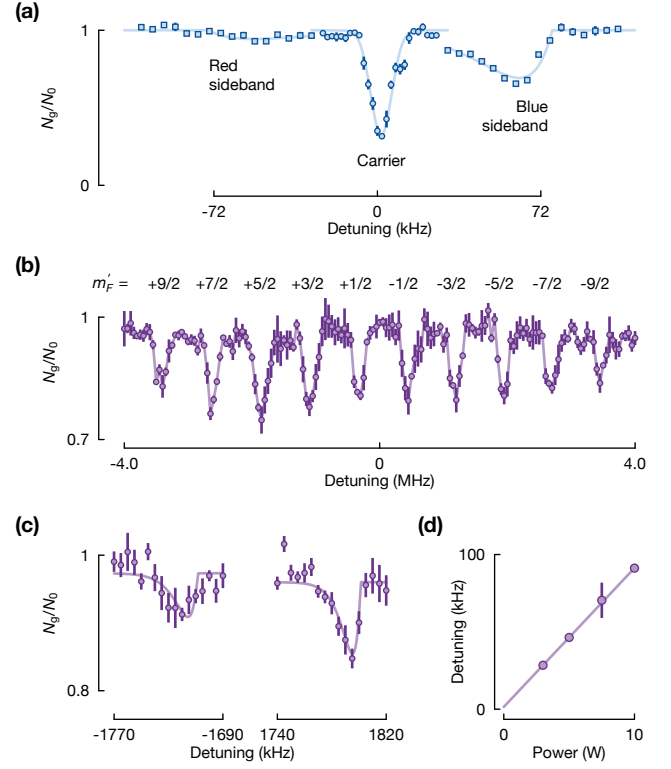


FIG. 8. (a) Motional sideband spectrum of the  $^1\text{S}_0-^3\text{P}_2$  ( $m_J = 1$ ) transition in  $^{88}\text{Sr}$  in a magic 1D optical lattice. The sidebands (squares) are probed with a factor of ten longer interrogation time than the carrier (dots). From the relative amplitude of the blue sideband to the red sideband, we extract a ground state fraction of 84 %. Markers, error bars, and solid lines are as in Fig. 4. (b) Spectrum of the  $^1\text{S}_0-^3\text{P}_2$   $F = 9/2$  transition in  $^{87}\text{Sr}$  in a bias magnetic field of 3 G. The markers represent an average of 3 measurements, and the error bars are the standard error of the mean. The solid lines serve as a guide to the eye. (c) Example of spectroscopic measurements for the determination of the  $^1\text{S}_0-^3\text{P}_2$  transition frequency in  $^{87}\text{Sr}$ . Here, we excite the atoms to the  $m_F = \pm 9/2$  states, within an optical lattice of a power of 5 W. The markers represent an average of 5 measurements, and the error bars the standard error of the mean. The solid lines are fits to the expected ac-Stark-shift-broadened line shape. (d) Average detuning of the  $^1\text{S}_0-^3\text{P}_2$ ,  $F = 9/2, m_F = \pm 9/2$  transitions as a function of lattice power. The solid line is a linear fit, from which we extract the zero-crossing to obtain the absolute transition frequency.

where  $y_0$  is the baseline of the spectrum,  $\delta$  is the detuning,  $\delta_0$  is the resonance frequency without the effect of the light shift, and  $\Theta$  is the Heaviside function. This line-shape can be used to describe both motional sidebands in Fig. 4 and Fig. 8(a), as well as the carrier in a strongly non-magic lattice in Fig. 5(b) and Fig. 8(c).

For lines where the dominant broadening mechanism is not the differential ac Stark shift – that is, for carrier transitions close to magic conditions – we instead use a symmetric function, taking the center as the resonance frequency. For our experimental conditions, we find that

these lines are best described by a Gaussian, as in the Carrier in Fig. 4 and Fig. 8(a), as well as Fig. 5(c).

*Sideband spectra.* — We characterize our optical lattice by measuring the frequencies of the motional sidebands of the  $^1S_0$ - $^3P_2$  ( $m_J = 1$ ) transition. Here, we achieve the magic condition with the magnetic field oriented along the  $-z$ -axis and using a lattice polarization with  $0.09 \pi$  ellipticity (see main text). By fitting the sidebands to Eq. (C1), we extract the sideband frequencies for various lattice powers. Under the assumption of a full lattice contrast (that is, the full optical power contributes to the trap frequency), we can estimate the  $1/e^2$  waist of the optical lattice to be  $\sim 144 \mu\text{m}$ . This waist is an upper bound since, realistically, the lattice contrast is expected to be reduced by experimental imperfections, such as finite mirror reflectivities.

A typical spectrum in a magic 5 W lattice is shown in Fig. 8(a). The red sideband is strongly suppressed compared to the blue sideband, showing that the atomic sample is cooled close to the vibrational ground state of the optical lattice [58]. From the relative amplitudes of the two sidebands, we extract a ground state fraction of 84%, consistent with a temperature of  $1.8 \mu\text{K}$  [75].

$^{88}\text{Sr}$  *absolute frequency determination and error budget.* — We extract the absolute transition frequency in  $^{88}\text{Sr}$  from spectroscopy of the  $m_J = 0$  transition at the magic condition, as presented in Fig. 4. We beat the spectroscopy laser, set to the carrier resonance condition, with a frequency comb to acquire an absolute frequency measurement. We estimate the systematic shifts due to light shift and density shift – from a set of additional measurements with the atom number reduced by an order of magnitude – to be negligible.

The statistical uncertainties from the estimation of the spectral line center and from the beat note with the comb are 27 Hz and 22 Hz, respectively, resulting in an overall statistical uncertainty of  $\delta\nu_{\text{stat}} = 35 \text{ Hz}$ .

Because the  $\Delta m_J = 0$  transition is insensitive to the first-order Zeeman effect, contributions from the magnetic field uncertainty enter only into the light shift, due to its effect on the magic condition. As the FWHM of the line is slightly larger than 2 kHz, we take 5 kHz as a conservative bound on the sum of possible residual light-shifts and density shifts.

Summing up the uncertainties, we obtain for  $^{88}\text{Sr}$  an absolute transition frequency of  $(446, 647, 242, 704 \pm 0.04_{\text{stat}} \pm 5_{\text{sys}}) \text{ kHz}$ .

$^{87}\text{Sr}$  *absolute frequency determination and error budget.* — Measuring the absolute frequency for  $^{87}\text{Sr}$  is more involved than for  $^{88}\text{Sr}$ . To eliminate the influence of the magnetic field, we sample two  $m_F$  states with opposite signs, such as  $m_F = \pm 9/2$ , shown in Fig 8(b). Finding magic conditions for these states was beyond the scope of this work, but we reached a condition close to magic for both states and performed a sequence of measurements with multiple lattice powers. Taking the average of the two frequencies for each lattice power, and extrapolating it to zero lattice power allows us to ex-

trapolate to zero light shift. As for  $^{88}\text{Sr}$ , we obtain the absolute transition frequency by beating the laser with a frequency comb. Finally, we apply a density correction using a set of measurements with a reduced number of atoms.

Taking measurements of the  $m_F = \pm 9/2$  states in the  $F = 9/2$  manifold close to magic conditions, shown in Fig 8(c), we observe the expected linear behavior as a function of the lattice power, as shown in Fig 8(d). We estimate a statistical uncertainty of 5 kHz on the intercept, that is, on the extrapolation to zero power. We estimate that the contributions of magnetic field and lattice power to the uncertainty are much smaller. The contribution from the beat note with the comb is once again sub-100 Hz and can be neglected.

By testing for density shifts at several lattice powers, we observe effects of up to 40 kHz. As a conservative bound, we take 60 kHz as the bound on the systematic uncertainty due to the density correction.

Therefore, we obtain for  $^{87}\text{Sr}$  a transition frequency to the  $F = 9/2$  state of  $(446, 647, 798, 423 \pm 5_{\text{stat}} \pm 60_{\text{sys}}) \text{ kHz}$ .

The hyperfine structure of the  $^3P_2$  state in  $^{87}\text{Sr}$  was measured to better than 10 kHz in Ref. [76]. Using this data, we can estimate the transition frequencies to all other  $F$  states and the center of gravity of the lines. We performed measurements of the transitions to the other hyperfine states with similar or larger uncertainties, and the frequencies agree with Ref. [76] within the error bars.

*Isotope shift.* — We can estimate the frequency difference between the transitions in the two isotopes simply by subtracting the frequency measurements performed with the frequency comb. Additionally, we can directly compare the different frequency shifts we applied to the probe beam between subsequent measurements for the two isotopes. Both estimates agree within a few kHz.

The  $F = 9/2$  state is 618.65 MHz blue detuned from the line's center of gravity [76]. Therefore, the isotope shift is  $\nu(^{88}\text{Sr}) - \nu(^{87}\text{Sr}) = +62.93(6) \text{ MHz}$ .

## Appendix D: Polarizability

*General expression.* — Here, we theoretically investigate the polarizability of the  $^3P_2$  state. The dynamic dipole polarizability  $\alpha_i$  of an atomic state  $|i\rangle$  can be decomposed into a scalar polarizability  $\alpha_i^s$ , a vector polarizability  $\alpha_i^v$ , and a tensor polarizability  $\alpha_i^t$  [20, 22, 62]

$$\begin{aligned} \alpha_i = & \alpha_i^s \\ & + \alpha_i^v \sin(2\gamma) \frac{m_i}{2J_i} \\ & + \alpha_i^t \frac{3 \cos^2(\beta) - 1}{2} \frac{3m_{J_i}^2 - J_i(J_i + 1)}{2J_i(2J_i - 1)}, \end{aligned} \quad (\text{D1})$$

where  $\gamma$  is the ellipticity angle of the polarization [20, 63] and  $\cos \beta$  is the projection of the polarization vector onto

TABLE II. The required information for calculating the polarizability of  $5s^2$   $^1S_0$  state and  $5s5p$   $^3P_2$  state of  $^{88}\text{Sr}$ . The energies and matrix elements of the different transitions are taken from Refs. [77] and [60, 78], respectively. The contributions to scalar  $\alpha_i^s(\lambda_0)$ , vector  $\alpha_i^v(\lambda_0)$  and tensor polarizability  $\alpha_i^t(\lambda_0)$  are calculated based on those values at  $\lambda_0 = 1064$  nm. *Other* refers to contributions to the scalar polarizability from states which are not listed explicitly and *Core* refers to the contribution to the polarizability from the closed electron shells of the atom. The units contain the electron charge  $e$ , the Bohr radius  $a_0$ , and the atomic unit of polarizability 1 a.u. =  $4\pi\epsilon_0 a_0^3$ , where  $\epsilon_0$  is the vacuum permittivity.

State $k$	$\Delta E_{ki}$ (cm $^{-1}$ )	$\langle k D i\rangle$ ( $ea_0$ )	$\alpha_i^s(\lambda_0)$ (a.u.)	$\alpha_i^v(\lambda_0)$ (a.u.)	$\alpha_i^t(\lambda_0)$ (a.u.)
State $i = 5s^2$ $^1S_0$					
$5s5p$ $^3P_1$	14504	0.397	0.40	0	0
$5s5p$ $^1P_1$	21698	5.248	228.61	0	0
$5s6p$ $^3P_1$	33868	0.034	0.01	0	0
$5s6p$ $^1P_1$	34098	0.282	0.37	0	0
Other			5.8	0	0
Core			5.3	0	0
<b>Total</b>		<b>240.49</b>	<b>0</b>	<b>0</b>	
State $i = 5s5p$ $^3P_2$					
$5s4d$ $^3D_1$	3260	0.6021	-0.45	3.85	0.45
$5s4d$ $^3D_2$	3320	2.331	-6.83	19.33	-6.83
$5s4d$ $^3D_3$	3421	5.530	-39.95	-219.52	11.41
$5s4d$ $^1D_2$	5251	0.102	-0.03	0.05	-0.03
$5s6s$ $^3S_1$	14140	4.521	75.78	-151.10	-75.78
$5s5d$ $^1D_2$	19829	0.365	0.25	-0.12	0.25
$5s5d$ $^3D_1$	20108	0.460	0.39	-0.55	-0.39
$5s5d$ $^3D_2$	20123	1.956	7.12	-3.32	7.12
$5s5d$ $^3D_3$	20146	4.994	46.30	43.20	-13.23
$5p^2$ $^3P_1$	20502	2.992	16.18	-22.25	-16.18
$5p^2$ $^3P_2$	20776	5.119	46.41	-21.00	46.41
$5p^2$ $^1D_2$	22062	0.682	0.75	-0.32	0.75
$5s7s$ $^3S_1$	22526	1.264	2.51	-3.15	-2.51
Other			43.1		0.34
Core			5.6		
<b>Total</b>		<b>197.14</b>	<b>-354.90</b>	<b>-48.56</b>	

the quantization axis. The ellipticity angle  $\gamma$  is defined as [20, 63]

$$\hat{\epsilon}_1 = \hat{\epsilon}_{1,1} \cos(\gamma) + i \hat{\epsilon}_{1,2} \sin(\gamma), \quad (\text{D2})$$

where  $\hat{\epsilon}_{1,1}$ ,  $\hat{\epsilon}_{1,2}$  are orthogonal vectors spanning the plane perpendicular to lattice propagation direction  $\mathbf{k}_1$ . We note that rotating the polarization ellipse within this plane does not affect the ellipticity angle  $\gamma$ , and thus does not affect the polarizability. Hence, we are not sensitive to the exact choice of  $\hat{\epsilon}_{1,1}$ ,  $\hat{\epsilon}_{1,2}$ . The quantization axis is assumed to be defined by a strong external magnetic field pointing along the  $z$ -axis.

The scalar polarizability of the state  $|i\rangle$  with angular momentum  $J_i$  at the light frequency  $\omega$  can be calculated

with [61, 62]

$$\alpha_i^s = \frac{1}{3(2J_i + 1)} \sum_k \frac{2}{\hbar} \frac{|\langle k|D|i\rangle|^2 \omega_{ki}}{\omega_{ki}^2 - \omega^2} + \alpha_i^c. \quad (\text{D3})$$

We sum over the dipole-allowed transitions to states  $|k\rangle$  with the corresponding dipole matrix element  $\langle k|D|i\rangle$ , and the transition frequency  $\omega_{ki} \equiv (E_k - E_i)/\hbar = \Delta E_{ki}/\hbar$ . Here,  $\alpha_i^c$  is the contribution of the core electrons to the scalar polarizability, where Ref. [78] provided us with a calculated value listed in Tab. II. The vector and the tensor polarizabilities are given by

$$\alpha_i^v = -\sqrt{\frac{6J_i}{(J_i + 1)(2J_i + 1)}} \sum_k (-1)^{J_i + J_k + 1} \quad (\text{D4})$$

$$\times \left\{ \begin{array}{ccc} 1 & 1 & 1 \\ J_i & J_k & J_i \end{array} \right\} \frac{|\langle k|D|i\rangle|^2}{\hbar} \left( \frac{1}{\omega_{ki} - \omega} - \frac{1}{\omega_{ki} + \omega} \right),$$

$$\alpha_i^t = -\sqrt{\frac{10J_i(2J_i - 1)}{3(J_i + 1)(2J_i + 1)(2J_i + 3)}} \quad (\text{D5})$$

$$\times \sum_k (-1)^{J_i + J_k} \left\{ \begin{array}{ccc} 1 & 2 & 1 \\ J_i & J_k & J_i \end{array} \right\} \frac{2}{\hbar} \frac{|\langle k|D|i\rangle|^2 \omega_{ki}}{\omega_{ki}^2 - \omega^2}.$$

$^1S_0$ - $^3P_2$  transition magic and tune-out wavelengths. — Using the matrix elements listed in Tab. II we can calculate the polarizability of the  $^1S_0$  and  $^3P_2$  states for different trapping light polarizations, as a function of the trapping wavelength, as shown in Fig. 9.

In Fig. 9(a), we plot the polarizabilities of the ground state and the Zeeman sublevels of the  $^3P_2$  state in the range of 800 nm to 1150 nm. We find that the  $^1S_0$ - $^3P_2$   $\Delta m_J = 0$  ( $\Delta m_J = \pm 1$ ) transition experiences a vanishing differential ac Stark shift at 1081(1) nm (994(1) nm) for  $\pi$ -polarized light. These magic wavelengths could be used for further precision spectroscopy on the  $^1S_0$ - $^3P_2$  transition in  $^{88}\text{Sr}$ .

In Fig. 9(b), we show the polarizability of the  $^3P_2$   $m_J = 0$  state for  $\pi$ -polarized light in the range of 550 nm to 800 nm. Here we can observe a so-called tune-out wavelength [22] at 679(2) nm, where the polarizability vanishes. The tune-out wavelength can be used to generate highly state-dependent optical traps with applications in quantum computing and quantum simulation [35, 65].

*Calculated magic conditions at 1064 nm.* — In this work, we did not vary the trap wavelength, but rather modified the trap polarization. This method allows finding magic conditions while choosing trapping wavelength based on other technical considerations. In our case, we use 1064 nm, a wavelength in which lasers with high optical power and low intensity noise are readily available.

For this reason, we are interested in the differential polarizability between the  $^1S_0$  state ( $g$ ) and a certain

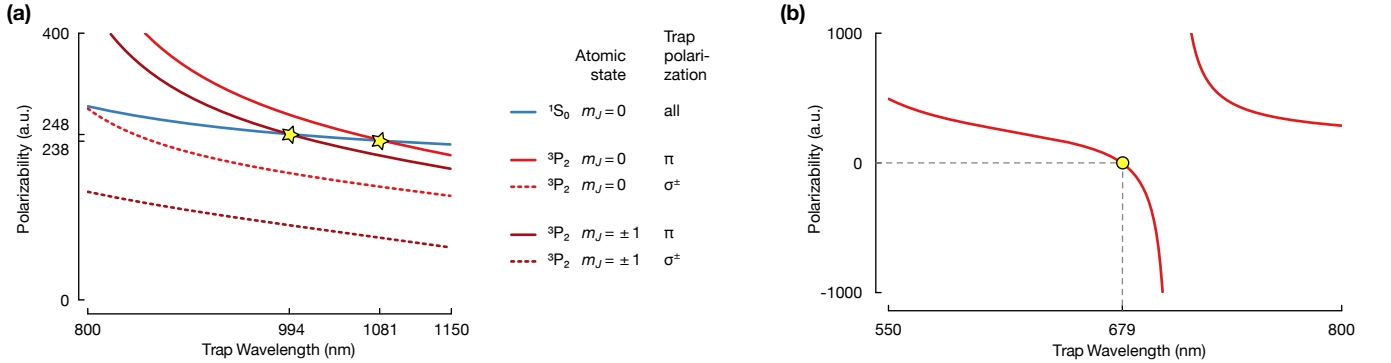


FIG. 9. (a) Polarizability of the  $^1\text{S}_0$   $m_J = 0$  and  $^3\text{P}_2$   $m_J = 0, \pm 1$  states for  $\pi$ - and  $\sigma^\pm$ -polarization as a function of the wavelength. The  $^1\text{S}_0$ - $^3\text{P}_2$   $\Delta = 0$  ( $\Delta = \pm 1$ ) transition experiences a vanishing differential stark shift for  $\pi$ -polarized light at 1081(1) nm (994(1) nm) (marked with a star). (b) Polarizability of the  $^3\text{P}_2$   $m_J = 0$  state as a function of the wavelength for  $\pi$ -polarized light. At 679(2) nm, the polarizability of this state vanishes. This wavelength is the so-called  $^3\text{P}_2$  tune-out wavelength (marked with a circle).

$^3\text{P}_2$   $m_J$  state ( $e$ ), given by

$$\Delta\alpha = \alpha_g^s - \left( \alpha_e^s + \frac{m_J}{2J} \sin(2\gamma_0) \alpha_e^v \right. \\ \left. + \frac{3\cos^2(\beta) - 1}{2} \frac{3m_J^2 - J(J+1)}{2J(2J-1)} \alpha_e^t \right), \quad (\text{D6})$$

where  $J = 2$  and  $m_J$  refer to the angular momentum of  $e$ . Using the values from Tab. II, we can thus extract the magic conditions for the scenarios of interest.

First, we consider the  $^3\text{P}_2$   $m_J = 0$  state. For this state, the vector polarizability vanishes. We can therefore use a linear polarization, and tune its orientation relative to quantization axis ( $\beta$ ) to modify the tensor polarizability. We find that the polarizability vanishes for the magic angle value of  $\beta_0 = 0.089\pi$ .

Second, we consider the  $^3\text{P}_2$   $m_J = 1$  state, and assume that the trapping light is parallel to the quantization axis. As described in Sec. IV, these are the conditions required for local addressing. Here,  $\beta = \pi/2$ , and the contribution of the tensor polarizability is constant. Hence, we tune the ellipticity angle  $\gamma$  and thereby the vector polarizability to find the magic condition. The polarizability vanishes for the magic ellipticity value of  $\gamma_0 = 0.108\pi$ .

*Experimental determination of magic ellipticity.* — Here we describe the determination of magic ellipticity shown in Fig. 5. In our experimental characterization of the vector ac Stark shift, we can only measure the differential ac Stark shift between the  $^1\text{S}_0$  state and the  $^3\text{P}_2$  state. The differential ac Stark shift  $\Delta\nu$  and the differential polarizability  $\Delta\alpha$  are connected by

$$\Delta\nu = \frac{1}{2\epsilon_0 ch} \Delta\alpha I, \quad (\text{D7})$$

where  $h$  is Planck's constant,  $\epsilon_0$  the vacuum permittivity,  $c$  the speed of light, and  $I$  the trapping light intensity. For an optical lattice generated by a perfectly retro-reflected Gaussian beam,  $I = (8P)/(\pi w^2)$ , for a beam with total power  $P$  and waist  $w$ . Since the lattice intensity is subject to systematic errors from the unknown contrast of the lattice beams, we do not convert the experimentally obtained differential light shifts into polarizabilities. Instead we use our data to extract the magic angle  $\gamma_0$  that is insensitive to the intensity calibration.

To do so, we measured spectra for each value of the ellipticity angle at lattice powers of 2.5 W, 5 W, 7.5 W, and 10 W, with some examples shown in Figs. 5(b) and (c). From each spectrum, we extract the transition frequency, and fitted the measured points to a function with independent linear coefficients for each ellipticity value, but a common intercept, with part of the data shown in the inset of Fig. 5(d).

Considering the linear coefficients as a function of  $\gamma$ , we extract  $\gamma_0$  by fitting the change in differential Stark shift  $\Delta_{AC}$  with lattice power  $P$  using

$$\frac{d\Delta_{AC}}{dP} = a_0 [\sin(2\gamma) - \sin(2\gamma_0)], \quad (\text{D8})$$

where  $a_0$  describes the amplitude of the curve, as shown in Fig. 5(d). With this parametrization, the uncertainty from the intensity calibration is contained entirely within  $a_0$ .

The largest uncertainty in our data arises from the calibration of the ellipticity angle. We used a commercial polarimeter to measure the polarization with an error of  $\pm 0.005\pi$ . Due to possible imperfect alignment while measuring the polarization we conservatively estimated the uncertainty as  $\Delta\gamma = \pm 0.01\pi$ . Our fit uncertainty is thus mostly determined by the error on the  $x$ -axis and not by errors on the  $y$ -axis.

---

\* sebastian.blatt@mpq.mpg.de

[1] T. Bothwell, C. J. Kennedy, A. Aeppli, D. Kedar, J. M. Robinson, E. Oelker, A. Staron, and J. Ye, Resolving the gravitational redshift across a millimetre-scale atomic sample, *Nature* **602**, 420 (2022).

[2] X. Zheng, J. Dolde, V. Lochab, B. N. Merriman, H. Li, and S. Kolkowitz, Differential clock comparisons with a multiplexed optical lattice clock, *Nature* **602**, 425 (2022).

[3] L. Sonderhouse, C. Sanner, R. B. Hutson, A. Goban, T. Bilitewski, L. Yan, W. R. Milner, A. M. Rey, and J. Ye, Thermodynamics of a deeply degenerate SU ( $N$ )-symmetric Fermi gas, *Nature Physics* **16**, 1216 (2020).

[4] H. Ozawa, S. Taie, Y. Takasu, and Y. Takahashi, Antiferromagnetic Spin Correlation of SU( $N$ ) Fermi Gas in an Optical Superlattice, *Physical Review Letters* **121**, 225303 (2018).

[5] F. Schäfer, T. Fukuoka, S. Sugawa, Y. Takasu, and Y. Takahashi, Tools for quantum simulation with ultracold atoms in optical lattices, *Nature Reviews Physics* **2**, 411 (2020).

[6] N. Schine, A. W. Young, W. J. Eckner, M. J. Martin, and A. M. Kaufman, Long-lived Bell states in an array of optical clock qubits, *Nature Physics* **18**, 1067 (2022).

[7] I. S. Madjarov, J. P. Covey, A. L. Shaw, J. Choi, A. Kale, A. Cooper, H. Pichler, V. Schkolnik, J. R. Williams, and M. Endres, High-fidelity entanglement and detection of alkaline-earth Rydberg atoms, *Nature Physics* **16**, 857 (2020).

[8] D. Okuno, Y. Nakamura, T. Kusano, Y. Takasu, N. Takei, H. Konishi, and Y. Takahashi, High-resolution spectroscopy and single-photon Rydberg excitation of reconfigurable ytterbium atom tweezer arrays utilizing a metastable state, arXiv:2204.07995 (2022).

[9] A. W. Young, W. J. Eckner, W. R. Milner, D. Kedar, M. A. Norcia, E. Oelker, N. Schine, J. Ye, and A. M. Kaufman, Half-minute-scale atomic coherence and high relative stability in a tweezer clock, *Nature* **588**, 408 (2020).

[10] G. E. Marti, R. B. Hutson, A. Goban, S. L. Campbell, N. Poli, and J. Ye, Imaging Optical Frequencies with 100  $\mu$ Hz Precision and 1.1  $\mu$ m Resolution, *Physical Review Letters* **120**, 103201 (2018).

[11] S. L. Campbell, R. Hutson, G. Marti, A. Goban, N. Darkwah Oppong, R. McNally, L. Sonderhouse, J. Robinson, W. Zhang, B. Bloom, *et al.*, A fermi-degenerate three-dimensional optical lattice clock, *Science* **358**, 90 (2017).

[12] I. I. Sobelman, *Atomic spectra and radiative transitions* (Springer Science & Business Media, 2012).

[13] G. Ferrari, P. Cancio, R. Drullinger, G. Giusfredi, N. Poli, M. Prevedelli, C. Toninelli, and G. M. Tino, Precision frequency measurement of visible intercombination lines of strontium, *Physical Review Letters* **91**, 243002 (2003).

[14] T. Nicholson, S. Campbell, R. Hutson, G. Marti, B. Bloom, R. McNally, W. Zhang, M. Barrett, M. Safranova, G. Strouse, W. Tew, and J. Ye, Systematic evaluation of an atomic clock at  $2 \times 10^{-18}$  total uncertainty, *Nat. Commun.* **6**, 6896 (2015).

[15] A. V. Taichenachev, V. I. Yudin, C. W. Oates, C. W. Hoyt, Z. W. Barber, and L. Hollberg, Magnetic Field-Induced Spectroscopy of Forbidden Optical Transitions with Application to Lattice-Based Optical Atomic Clocks, *Physical Review Letters* **96**, 083001 (2006).

[16] T. Takano, R. Mizushima, and H. Katori, Precise determination of the isotope shift of 88sr-87sr optical lattice clock by sharing perturbations, *Applied Physics Express* **10**, 072801 (2017).

[17] F. Riehle, P. Gill, F. Arias, and L. Robertsson, The CIPM list of recommended frequency standard values: guidelines and procedures, *Metrologia* **55**, 188 (2018).

[18] R. H. Garstang, Magnetic Quadrupole Line Intensities, *Astrophysical Journal* **148**, 579 (1967).

[19] M. M. Boyd, T. Zelevinsky, A. D. Ludlow, S. Blatt, T. Zanon-Willette, S. M. Foreman, and J. Ye, Nuclear spin effects in optical lattice clocks, *Physical Review A* **76**, 022510 (2007).

[20] A. Cooper, J. P. Covey, I. S. Madjarov, S. G. Porsev, M. S. Safranova, and M. Endres, Alkaline-earth atoms in optical tweezers, *Physical Review X* **8**, 041055 (2018).

[21] M. A. Norcia, A. W. Young, and A. M. Kaufman, Microscopic Control and Detection of Ultracold Strontium in Optical-Tweezer Arrays, *Physical Review X* **8**, 041054 (2018).

[22] A. Heinz, A. J. Park, N. Šantić, J. Trautmann, S. G. Porsev, M. S. Safranova, I. Bloch, and S. Blatt, State-dependent optical lattices for the strontium optical qubit, *Physical Review Letters* **124**, 203201 (2020).

[23] M. Takamoto, F.-L. Hong, R. Higashi, and H. Katori, An optical lattice clock, *Nature* **435**, 321 (2005).

[24] A. Brusch, R. Le Targat, X. Baillard, M. Fouché, and P. Lemonde, Hyperpolarizability Effects in a Sr Optical Lattice Clock, *Physical Review Letters* **96**, 103003 (2006).

[25] A. D. Ludlow, M. M. Boyd, T. Zelevinsky, S. M. Foreman, S. Blatt, M. Notcutt, T. Ido, and J. Ye, Systematic Study of the  $^{87}\text{Sr}$  Clock Transition in an Optical Lattice, *Physical Review Letters* **96**, 033003 (2006).

[26] M. Bishop, M. J. Martin, M. D. Swallows, C. Benko, Y. Lin, G. Quéméner, A. M. Rey, and J. Ye, Inelastic collisions and density-dependent excitation suppression in a  $^{87}\text{Sr}$  optical lattice clock, *Physical Review A* **84**, 052716 (2011).

[27] J. A. Muniz, D. J. Young, J. R. K. Cline, and J. K. Thompson, Cavity-QED measurements of the  $^{87}\text{Sr}$  millihertz optical clock transition and determination of its natural linewidth, *Physical Review Research* **3**, 023152 (2021).

[28] W. F. McGrew, X. Zhang, R. J. Fasano, S. A. Schäffer, K. Beloy, D. Nicolodi, R. C. Brown, N. Hinkley, G. Miliani, M. Schioppo, T. H. Yoon, and A. D. Ludlow, Atomic clock performance enabling geodesy below the centimetre level, *Nature* **564**, 87 (2018).

[29] E. Oelker, R. B. Hutson, C. J. Kennedy, L. Sonderhouse, T. Bothwell, A. Goban, D. Kedar, C. Sanner, J. M. Robinson, G. E. Marti, D. G. Matei, T. Legero, M. Giunta, R. Holzwarth, F. Riehle, U. Sterr, and J. Ye, Demonstration of  $4.8 \times 10^{-17}$  stability at 1 s for two independent optical clocks, *Nature Photonics* **13**, 714 (2019).

[30] C. Lisdat, J. S. R. V. Winfred, T. Middelmann, F. Riehle, and U. Sterr, Collisional Losses, Decoherence, and Frequency Shifts in Optical Lattice Clocks with Bosons, *Physical Review Letters* **103**, 090801 (2009).

[31] T. Akatsuka, M. Takamoto, and H. Katori, Three-dimensional optical lattice clock with bosonic  $^{88}\text{Sr}$  atoms, *Physical Review A* **81**, 023402 (2010).

[32] S. B. Koller, J. Grotti, S. Vogt, A. Al-Masoudi, S. Dörscher, S. Häfner, U. Sterr, and C. Lisdat, Transportable Optical Lattice Clock with  $7 \times 10^{-17}$  Uncertainty, *Physical Review Letters* **118**, 073601 (2017).

[33] T. Ido and H. Katori, Recoil-Free Spectroscopy of Neutral Sr Atoms in the Lamb-Dicke Regime, *Physical Review Letters* **91**, 053001 (2003).

[34] M. Yasuda and H. Katori, Lifetime measurement of the  $^3\text{P}_2$  metastable state of strontium atoms, *Physical Review Letters* **92**, 153004 (2004).

[35] A. J. Daley, M. M. Boyd, J. Ye, and P. Zoller, Quantum computing with alkaline-earth-metal atoms, *Physical Review Letters* **101**, 170504 (2008).

[36] K. Shibata, S. Kato, A. Yamaguchi, S. Uetake, and Y. Takahashi, A scalable quantum computer with ultra-narrow optical transition of ultracold neutral atoms in an optical lattice, *Applied Physics B* **97**, 753 (2009).

[37] S. Kato, K. Shibata, R. Yamamoto, Y. Yoshikawa, and Y. Takahashi, Optical magnetic resonance imaging with an ultra-narrow optical transition, *Applied Physics B* **108**, 31 (2012).

[38] K. Shibata, R. Yamamoto, Y. Seki, and Y. Takahashi, Optical spectral imaging of a single layer of a quantum gas with an ultranarrow optical transition, *Physical Review A* **89**, 031601 (2014).

[39] R. Yamamoto, J. Kobayashi, T. Kuno, K. Kato, and Y. Takahashi, An ytterbium quantum gas microscope with narrow-line laser cooling, *New Journal of Physics* **18**, 023016 (2006).

[40] W. S. Bakr, J. I. Gillen, A. Peng, S. Fölling, and M. Greiner, A quantum gas microscope for detecting single atoms in a Hubbard-regime optical lattice, *Nature* **462**, 74 (2009).

[41] J. F. Sherson, C. Weitenberg, M. Endres, M. Cheneau, I. Bloch, and S. Kuhr, Single-atom-resolved fluorescence imaging of an atomic Mott insulator, *Nature* **467**, 68 (2010).

[42] S. Kato, S. Sugawa, K. Shibata, R. Yamamoto, and Y. Takahashi, Control of resonant interaction between electronic ground and excited states, *Physical Review Letters* **110**, 173201 (2013).

[43] A. Yamaguchi, S. Uetake, D. Hashimoto, J. M. Doyle, and Y. Takahashi, Inelastic Collisions in Optically Trapped Ultracold Metastable Ytterbium, *Physical Review Letters* **101**, 233002 (2008).

[44] O. Onishchenko, S. Pyatchenkov, A. Urech, C. C. Chen, S. Bennetts, G. A. Siviloglou, and F. Schreck, Frequency of the ultranarrow  $^1\text{S}_0 - ^3\text{P}_2$  transition in  $^{87}\text{Sr}$ , *Physical Review A* **99**, 1 (2019).

[45] I. V. Hertel and C.-P. Schulz, *Atoms, molecules and optical physics* (Springer, 2014).

[46] W. R. Johnson, *Atomic structure theory* (Springer, 2007).

[47] W. E. Lamb, R. R. Schlicher, and M. O. Scully, Matter-field interaction in atomic physics and quantum optics, *Physical Review A* **36**, 2763 (1987).

[48] D. A. Varshalovich, A. N. Moskalev, and V. K. Kersonskii, *Quantum Theory of Angular Momentum* (World Scientific, Singapore, 1988).

[49] M. Mizushima,  $\delta s = \pm 1$  Magnetic Quadrupole Radiative Transitions in Atoms and Molecules, *Journal of the Physical Society of Japan* **21**, 2335 (1966).

[50] M. Auzinsh, D. Budker, and S. Rochester, *Optically polarized atoms: understanding light-atom interactions* (Oxford University Press, 2010).

[51] P. Lodahl, S. Mahmoodian, S. Stobbe, A. Rauschenbeutel, P. Schneeweiss, J. Volz, H. Pichler, and P. Zoller, Chiral quantum optics, *Nature* **541**, 473 (2017).

[52] S. A.-L. Schulz, A. A. Peshkov, R. A. Müller, R. Lange, N. Huntemann, C. Tamm, E. Peik, and A. Surzhykov, Generalized excitation of atomic multipole transitions by twisted light modes, *Physical Review A* **102**, 012812 (2020).

[53] C. T. Schmiegelow and F. Schmidt-Kaler, Light with orbital angular momentum interacting with trapped ions, *The European Physical Journal D* **66**, 1 (2012).

[54] C. T. Schmiegelow, J. Schulz, H. Kaufmann, T. Ruster, U. G. Poschinger, and F. Schmidt-Kaler, Transfer of optical orbital angular momentum to a bound electron, *Nature communications* **7**, 1 (2016).

[55] S. Snigirev, A. J. Park, A. Heinz, I. Bloch, and S. Blatt, Fast and dense magneto-optical traps for strontium, *Physical Review A* **99**, 063421 (2019).

[56] A. J. Park, J. Trautmann, N. Šantić, V. Klüsener, A. Heinz, I. Bloch, and S. Blatt, Cavity-enhanced optical lattices for scaling neutral atom quantum technologies to higher qubit numbers, *PRX Quantum* **3**, 030314 (2022).

[57] S. Schmid, G. Thalhammer, K. Winkler, F. Lang, and J. H. Denschlag, Long distance transport of ultracold atoms using a 1D optical lattice, *New Journal of Physics* **8**, 159 (2006).

[58] S. Blatt, J. W. Thomsen, G. K. Campbell, A. D. Ludlow, M. D. Swallows, M. J. Martin, M. M. Boyd, and J. Ye, Rabi spectroscopy and excitation inhomogeneity in a one-dimensional optical lattice clock, *Physical Review A* **80**, 052703 (2009).

[59] A. Traverso, R. Chakraborty, Y. N. Martinez de Escobar, P. G. Mickelson, S. B. Nagel, M. Yan, and T. C. Killian, Inelastic and elastic collision rates for triplet states of ultracold strontium, *Physical Review A* **79**, 060702 (2009).

[60] M. S. Safronova, S. G. Porsev, U. I. Safronova, M. G. Kozlov, and C. W. Clark, Blackbody-radiation shift in the Sr optical atomic clock, *Physical Review A* **87**, 012509 (2013).

[61] M. S. Safronova, Z. Zuhrianda, U. I. Safronova, and C. W. Clark, Extracting transition rates from zero-polarizability spectroscopy, *Physical Review A* **92**, 040501 (2015).

[62] F. L. Kien, P. Schneeweiss, and A. Rauschenbeutel, Dynamical polarizability of atoms in arbitrary light fields: general theory and application to cesium, *The European Physical Journal D* **67**, 1 (2013).

[63] P. Rosenbusch, S. Ghezali, V. A. Dzuba, V. V. Flambaum, K. Belyov, and A. Derevianko, ac Stark shift of the Cs microwave atomic clock transitions, *Physical Review A* **79**, 013404 (2009).

[64] C. Weitenberg, M. Endres, J. F. Sherson, M. Cheneau, P. Schaus, T. Fukuhara, I. Bloch, and S. Kuhr, Single-spin addressing in an atomic Mott insulator, *Nature* **471**, 319 (2011).

[65] A. J. Daley, Quantum computing and quantum simulation with group-II atoms, *Quantum Information Processing* **10**, 865 (2011).

[66] C. Gross and W. S. Bakr, Quantum gas microscopy for single atom and spin detection, *Nature Physics* **17**, 1316 (2021).

[67] M. Born and E. Wolf, *Principles of Optics: Electromagnetic Theory of Propagation, Interference and Diffraction of Light* (Elsevier, 2013).

[68] J. Sansonetti and G. Nave, Wavelengths, transition probabilities, and energy levels for the spectrum of neutral strontium (Sr I), *Journal of Physical and Chemical Reference Data* **39**, 033103 (2010).

[69] E. Haller, J. Hudson, A. Kelly, D. A. Cotta, B. Peaudecerf, G. D. Bruce, and S. Kuhr, Single-atom imaging of fermions in a quantum-gas microscope, *Nature Physics* **11**, 738 (2015).

[70] A. Pagano, S. Weber, D. Jaschke, T. Pfau, F. Meinert, S. Montangero, and H. P. Büchler, Error budgeting for a controlled-phase gate with strontium-88 Rydberg atoms, *Physical Review Research* **4**, 033019 (2022).

[71] J. D. Jackson, *Classical electrodynamics*, 3rd ed. (Wiley, 1999).

[72] M. Mizushima,  $\Delta s = \pm 1$  Magnetic Multipole Radiative Transitions, *Physical Review* **134**, A883 (1964).

[73] J. Léonard, M. Lee, A. Morales, T. M. Karg, T. Esslinger, and T. Donner, Optical transport and manipulation of an ultracold atomic cloud using focus-tunable lenses, *New Journal of Physics* **16**, 093028 (2014).

[74] Y. Bao, S. S. Yu, L. Anderegg, S. Burchesky, D. Gonzalez-Acevedo, E. Chae, W. Ketterle, K.-K. Ni, and J. M. Doyle, Fast optical transport of ultracold molecules over long distances (2022).

[75] M. McDonald, B. H. McGuyer, G. Z. Iwata, and T. Zelevinsky, Thermometry via Light Shifts in Optical Lattices, *Physical Review Letters* **114**, 023001 (2015).

[76] S. M. Heider and G. O. Brink, Hyperfine structure of  $^{87}\text{Sr}$  in the  $^3\text{P}_2$  metastable state, *Physical Review A* **16**, 1371 (1977).

[77] A. Kramida, Yu. Ralchenko, J. Reader, and and NIST ASD Team, NIST Atomic Spectra Database (ver. 5.8), [Online]. Available: <https://physics.nist.gov/asd> [10/30/2020]. National Institute of Standards and Technology, Gaithersburg, MD. (2020).

[78] M. S. Safronova, private communication (2022).